Bone Reports 22 (2024) 101783

Contents lists available at ScienceDirect

Bone Reports

journal homepage: www.elsevier.com/locate/bonr

Bone hierarchical organization through the lens of materials science: Present opportunities and future challenges

Chiara Micheletti, Furqan A. Shah *

Department of Biomaterials, Sahlgrenska Academy, University of Gothenburg, Gothenburg, Sweden

A R T I C L E I N F O

Keywords:
Bone
Biomaterials
Biomineralization
Electron microscopy
Spectroscopy
Materials science

A B S T R A C T

Multiscale characterization is essential to better understand the hierarchical architecture of bone and an array of analytical methods contributes to exploring the various structural and compositional aspects. Incorporating X-ray tomography, X-ray scattering, vibrational spectroscopy, and atom probe tomography alongside electron microscopy provides a comprehensive approach, offering insights into the diverse levels of organization within bone. X-ray scattering techniques reveal information about collagen-mineral spatial relationships, while X-ray tomography captures 3D structural details, especially at the microscale. Electron microscopy, such as scanning and transmission electron microscopy, extends resolution to the nanoscale, showcasing intricate features such as collagen fibril organization. Additionally, atom probe tomography achieves sub-nanoscale resolution and high chemical sensitivity, enabling detailed examination of bone composition. Despite various technical challenges, a correlative approach allows for a comprehensive understanding of bone material properties. Real-time investigations through in situ and *in operando* approaches shed light on the dynamic processes in bone. Recently developed techniques such as liquid, in situ transmission electron microscopy provide insights into calcium phosphate formation and collagen mineralization. Mechanical models developed in the effort to link structure, composition, and function currently remain oversimplified but can be improved. In conclusion, correlative analytical platforms provide a holistic perspective of bone extracellular matrix and are essential for unraveling the intricate interplay between structure and composition within bone.

1. Introduction

The extracellular matrix of bone is an exquisite material, at the same time tough and strong, lightweight, and able to repair itself when old or damaged. The remarkable ability of bone extracellular matrix to resist both non-recoverable deformation (strength) and fracture (toughness) is mainly owed to the hierarchical organization of the two main constituents, type I collagen fibrils and calcium phosphate mineral (Fratzl and Weinkamer, 2007; Ritchie et al., 2009). Hierarchical structure means that smaller building blocks progressively build up larger structures. In bone, this holds across length scales spanning several orders of magnitude, from molecular assemblies all the way up to the whole bone level (Reznikov et al., 2014a). Notably, such a hierarchical structure is preserved during bone remodeling cycles, and it is present not just in native tissue, but also in bone formed at biomaterial interfaces (Shah et al., 2019a).

At the molecular level, three collagen molecules intertwine into triple helices (tropocollagen), which self-organize in a quarter-staggered fashion generating ∼27 nm overlap and ∼ 40 nm gap zones, for an overall periodic D-spacing of ∼67 nm (Hodge and Petruska, 1963; Orgel et al., 2001). In 3D, they form fibrils of indeterminate length and diameters of 80–120 nm (Fratzl and Weinkamer, 2007; Reznikov et al., 2014a; Weiner et al., 1997), although values down to 20–50 nm have also been reported (McNally et al., 2012; Schwarcz, 2015; Grandfield et al., 2018; Lee et al., 2021; Micheletti et al., 2023). Of particular interest is the nano-composite formed once the collagen fibrils become mineralized, i.e., the *mineralized collagen fibril*, which is often labelled as the "building block" of bone (Reznikov et al., 2014a). Mineralization takes place both inside individual fibrils within the gap zones (intrafibrillar) (Weiner and Traub, 1986; Landis et al., 1993), and in the spaces between adjacent fibrils (inter−/extrafibrillar) (McNally et al., 2012; Schwarcz, 2015; Landis et al., 1996a; Pidaparti et al., 1996). It is currently unknown where mineralization begins in spatial relation to the fibrils, or whether intra- and extrafibrillar mineral are interconnected. Evidence in favor of an interconnection has been highlighted by Reznikov et al., who have shown that the mineral extends over multiple

---

* Corresponding author.
E-mail address: furqan.ali.shah@biomaterials.gu.se (F.A. Shah).

https://doi.org/10.1016/j.bonr.2024.101783
Received 31 December 2023; Received in revised form 20 June 2024; Accepted 22 June 2024
Available online 25 June 2024
2352-1872/© 2024 The Author(s). Published by Elsevier Inc. This is an open access article under the CC BY-NC-ND license (http://creativecommons.org/licenses/by-nc-nd/4.0/).

fibrils in a "crossfibrillar" mineralization fashion that is neither purely intra- nor extrafibrillar (Reznikov et al., 2018). On the other hand, we have recently demonstrated that mineral splaying multiple fibrils can be clearly seen in the extrafibrillar region only, while questions remain unanswered on an eventual direct connection between extrafibrillar and intrafibrillar compartments (Micheletti et al., 2023). It has been proposed that the physical structure of the collagen fibril directly influences intrafibrillar mineralization. For example, fetuin-A, which is an important inhibitor of apatite growth, is physically unable to enter the collagen fibril, and by selectively inhibiting apatite growth external to the fibril, leads to mineralization intrafibrillarly (Price et al., 2009).

Bone mineral is commonly described as a carbonate-substituted hydroxy(l)apatite (Skinner, 2005), although some authors have reported little-to-no-presence of hydroxyl (OH^-) groups in bone apatite (Pasteris et al., 2004). Bone mineral itself appears to be a hierarchical structure, being formed by smaller units that assemble into larger-order aggregates (Reznikov et al., 2018). While the habit of the smallest mineral subcomponents has been object of debate – are mineral particles needles

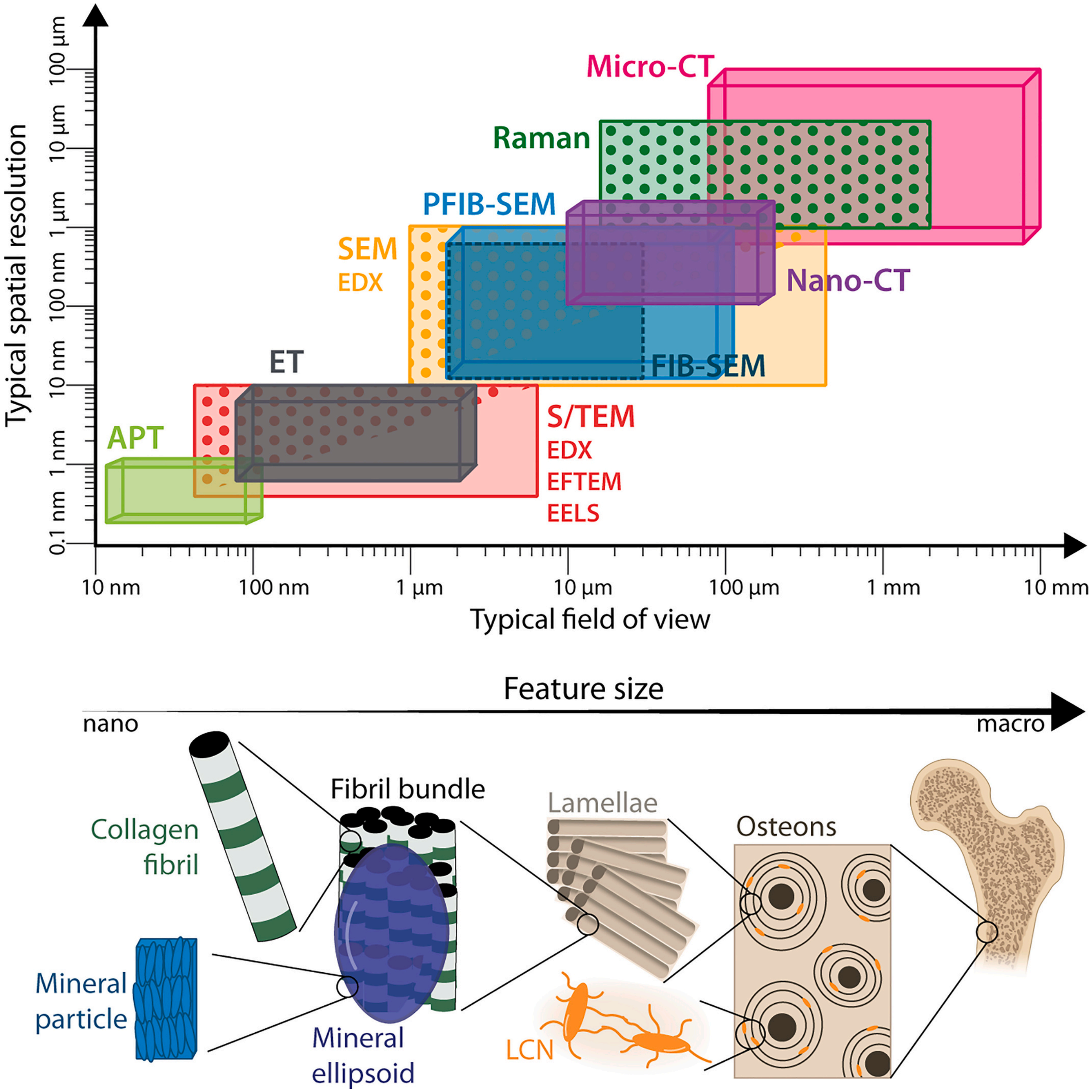
Typical spatial resolution
0.1 nm
1 nm
10 nm
100 nm
1 µm
10 µm
100 µm
Micro-CT
Raman
PFIB-SEM
SEM
EDX
Nano-CT
FIB-SEM
ET
APT
S/TEM
EDX
EFTEM
EELS
10 nm
100 nm
1 µm
10 µm
100 µm
1 mm
10 mm
Typical field of view
Feature size
nano
macro
Collagen fibril
Fibril bundle
Lamellae
Osteons
Mineral particle
Mineral ellipsoid
LCN

Fig. 1. Multiscale and multimodal characterization of bone. Typical spatial resolution vs. field of view of the main techniques described in this review (top) in relation to the hierarchical structure of bone (bottom). 2D and 3D techniques are shown as rectangles and cuboids, respectively. Spectroscopy techniques are marked with a dotted pattern. APT = atom probe tomography, CT = computed tomography, FIB = focused ion beam, PFIB = plasma FIB, SEM = scanning electron microscopy, S/TEM = scanning/transmission electron microscopy, EELS = electron energy-loss spectroscopy, EDX = energy-dispersive X-ray spectroscopy, EFTEM = energy-filtered TEM, LCN = lacuno-canalicular network.
[Adapted from Micheletti, PhD Thesis (Micheletti, 2023)]

or plates? – increasing evidence suggests that their final assembly has the geometrical shape of an ellipsoid only a few μm in size (Binkley et al., 2020; Buss et al., 2020). These structures have been variously referred to as "tesselles" (Buss et al., 2020, 2022) or "mineral (prolate) ellipsoids" (Binkley et al., 2020; Micheletti et al., 2022a), and "*pack against one another to form a congruent and contiguous mineral tessellation pattern*" (Buss et al., 2020), which has been termed as "crossfibrillar tessellation" (Buss et al., 2020).

At the microscale in lamellar bone, 2–3 μm bundles of mineralized collagen fibrils group themselves into "lamellae", which then form the different structural motifs found at the tissue level, i.e., trabeculae vs. osteons vs. circumferential lamellar bone (Reznikov et al., 2014a). In secondary osteons in cortical bone, lamellae are rings concentrically organized around the Haversian canal. Theories on the exact arrangement of collagen bundles within osteonal lamellae have often been revisited (see review by Mitchell et al. (Mitchell and van Heteren, 2016)), but there is a broad consensus on the rotated/twisted plywood architecture (Weiner et al., 1997; Wagermaier et al., 2006). At the macroscale, the main distinction concerns cortical vs. trabecular bone, the dense outer shell and porous interior compartment of whole bones, respectively.

Histology is the gold standard technique to study biological tissues. Bone is no exception. Important information on the metabolic state (e.g., healthy vs. necrotic), the organization at the tissue level (e.g., woven vs. lamellar), and the cellular and vascular elements of bone can be retrieved by examining appropriately stained histological sections. However, this is not suitable for a thorough investigation of the complex hierarchical architecture of bone, which, based on the research questions, may require higher spatial resolution, chemical characterization, three-dimensional (3D) visualization, etc. For such a task, a multiscale and multimodal characterization approach is more suitable. *Multiscale* refers to the need to encompass multiple hierarchical levels spanning multiple length scales (nano-micro-meso-macro). This in turn requires combining different techniques based on different probes (visible light, X-rays, electrons, etc.) and probe-matter interactions (absorption, emission, elastic/inelastic scattering, etc.) to retrieve structural and -compositional information, hence the term *multimodal*. Additionally, this characterization platform is also often multidimensional, i.e., based on both two- and three-dimensional (2D and 3D) data. Such a characterization approach integrates techniques commonly used in materials science, enriching the study of bone structure and composition through interdisciplinary collaboration that extends to and actively involves the biological and clinical communities. The necessity of adopting different tools stems from the fact that "no one size fits all", as a trade-off exists between spatial resolution and field of view (area/volume of material analyzed). This is exemplified in relation to bone structure (Fig. 1), to demonstrate that by combining several characterization techniques, we can access structural and compositional information across the entirety of bone architecture.

This review discusses several techniques used in such a multimodal and multiscale characterization platform of bone, covering basic working principles and example applications of both conventional and advanced techniques. The interested reader may further refer to existing technique-specific reviews on X-ray tomography (Müller, 2009; Peyrin et al., 2014) and X-ray scattering (Paris, 2008), scanning electron microscopy (SEM) (Shah et al., 2019b), including resin cast etching (Sato and Shah, 2023), focused ion beam (FIB)-SEM (Weiner et al., 2021), Fourier transform infrared (FTIR) and Raman spectroscopy (Taylor and Donnelly, 2020), and atom probe tomography (APT) (Grandfield et al., 2022). Instead, we aim to complement existing reviews on multiscale characterization of bone (Grandfield, 2015; Georgiadis et al., 2016; Binkley and Grandfield, 2017; Palmquist, 2018), specifically discussing current opportunities offered by this materials science-inspired characterization approach, highlighting the limitations, and addressing future challenges.

2. Using photons to gain structural information

2.1. Visible light microscopy and use of polarized light

The most immediate and accessible tool to obtain a magnified view of any material is the optical (visible light) microscope. Bone was indeed among the materials imaged by microscopy-pioneer Antonie van Leeuwenhoek at the turn of the 17th to 18th centuries (Leeuwenhoek, 1721). Perhaps the most widespread use of visible light in bone biology is together with histological analysis, where appropriate stains are selected to provide information on cellular and other tissue components, or on mineralization events through dynamic histology. An in-depth review of the application of histological and histomorphometric methods to bone is beyond the current scope. Light microscopy coupled with histological analyses was also fundamental to the discovery that bone forms a direct connection with certain implanted materials without any interposed connective tissue (Brånemark et al., 1977). This phenomenon, termed *osseointegration*, was in fact first defined as "a direct – *on light microscopic level* – contact between living bone and implant" (Albrektsson et al., 1981).

Even without any specific histological stains, polished bone samples can be inspected in reflection or in transmission mode, if thin enough, e.g., 100 ± 5 μm (Goldman et al., 1999), to observe features at the microscale such as osteonal lamellae, trabeculae and osteocyte lacunae. The use of polarized light microscopy in understanding bone on the extracellular matrix level is worth mentioning (Georgiadis et al., 2016; Bromage et al., 2003). By leveraging the birefringent nature and optical anisotropy of collagen, polarized light microscopy has been used, historically, to determine the orientation of collagen fibers, especially in compact bone (Boyde and Riggs, 1990) and osteons (Ascenzi and Bonucci, 1968) (Fig. 2A–B). Multiphoton imaging further enhances our understanding of bone microarchitecture. Techniques such as Second Harmonic Generation (SHG) directly visualize collagen alignment, while Third Harmonic Generation (THG) complements this by highlighting interfaces and structures such as the lacuno-canalicular network (LCN) (Genthial et al., 2017).

2.2. X-ray computed tomography: micro-CT and nano-CT

A higher spatial resolution when imaging with photons can be obtained with X-rays. A popular X-ray based, non-destructive technique to obtain 3D information on both shape/geometry and internal architecture is X-ray computed tomography (CT) (Withers et al., 2021). Originating from medical CT ("CAT scans"), micro-CT and nano-CT were developed to afford higher resolution ex vivo analyses of bone microstructure, usually in the 1–100 μm range for micro-CT and down to a few hundreds of nm for nano-CT in desktop instruments (Peyrin et al., 2014). Even higher resolutions can be achieved using monochromatic X-ray beams at synchrotron radiation sources, down to 10 nm (Withers et al., 2021). In both micro- and nano-CT, a sample placed between an X-ray source and a detector is axially rotated, usually for a complete 360° rotation, and a 2D radiography (X-ray projection images) is captured at each rotation step. The image contrast in the radiographs depends on the attenuation/absorption of X-rays, hence on density and thickness heterogeneities within the sample. The radiographs are combined by special algorithms (e.g., based on back-projection) to yield a 3D representation of the interior of the sample (Withers et al., 2021).

In this context, perhaps the most typical application of micro-CT is quantitative analysis of bone microarchitecture (Müller, 2009), for example, measuring parameters related to both cortical and trabecular bone, such as cortical and trabecular thickness, porosity in the trabecular compartment, trabecular separation and number, degree of anisotropy, etc. (Bouxsein et al., 2010) (Fig. 2C). This effectively makes it possible to extend traditional bone histomorphometry in 3D. Although strictly speaking micro-CT is for structural characterization only, some composition-related information can also be retrieved. This is

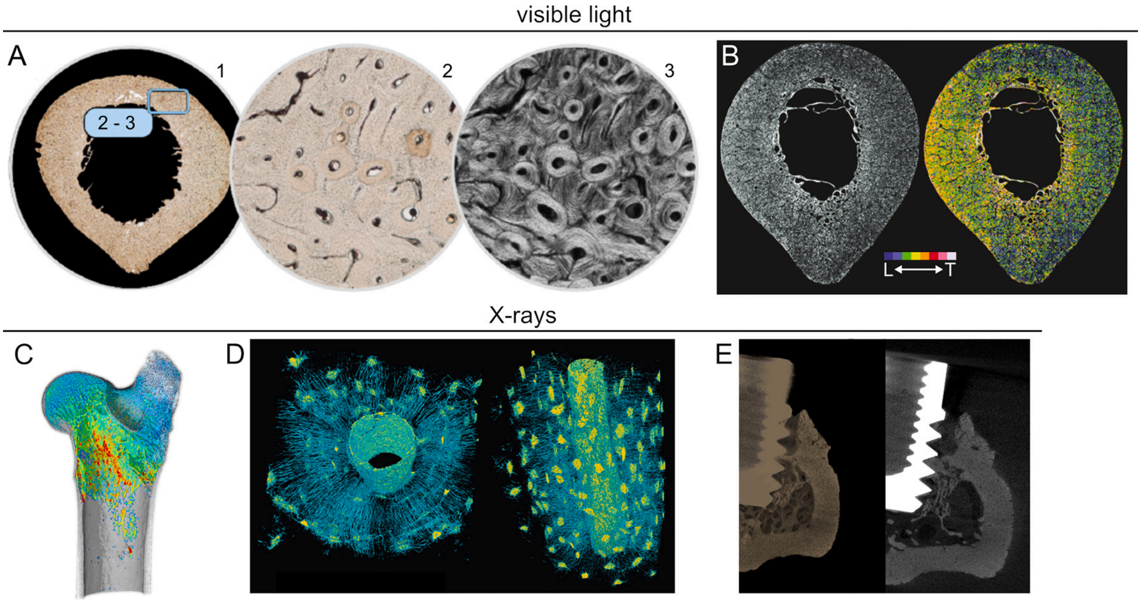

Fig. 2. Photon-based structural characterization. A) Visible (panels 1–2) and polarized light (panel 3) micrographs of a transverse cross-section of human femur [adapted from Stockhausen et al. (Stockhausen et al., 2021) with permission, Copyright 2021, American Chemical Society]. B) As-acquired and false-colored (from blue indicating longitudinal lamellae, L, to white indicating transverse lamellae, T) polarized light micrograph of mid-shaft human femur (transverse section) [adapted from Bromage et al. (2003) with permission, Copyright 2003, John Wiley & Sons]. C) Micro-CT reconstruction of sheep femur cropped to reveal internal trabecular architecture, color-coded based on thickness [adapted from ORS Dragonfly – Application Note on "Bone Analysis" module (Systems OR, 2019)]. D) 3D rendering of the LCN (blue: canaliculi; yellow: lacunae) in an osteon from a synchrotron CT reconstruction [adapted from Pacureanu et al. (2012) with permission, Copyright 2012, John Wiley & Sons]. E) 3D rendering (left) and reconstructed slice (right) of bone formed around a titanium implant acquired with micro-CT [image courtesy of Charlotte Primeau, University of Warwick].

accomplished by converting the grey-levels in the reconstruction into tissue mineral density using calibration standards containing hydroxy(l)apatite (Bouxsein et al., 2010). Other features at the microscale level such as the Haversian system (Bousson et al., 2004) and resorption spaces of basic multicellular units (Cooper et al., 2006) can also be characterized with micro/nano-CT. The higher spatial resolution of synchrotron CT opened the possibility to resolve smaller features, such as the LCN (Pacureanu et al., 2012) (Fig. 2D). While imaging of osteocyte lacune is now also possible with desktop instruments, visualizing the canaliculi remains non-trivial and requires optimized setups at synchrotron radiation facilities (Peyrin et al., 2014). Characterizing the LCN is challenging yet important, as osteocytes with their dendrites serve essential functions in mechanosensing, orchestrating bone modeling and remodeling (Bonewald, 2011).

X-ray CT has found applications also in the context of osseointegration, making it possible to evaluate bone growth in the peri-implant space in 3D and examine the microarchitecture of newly formed bone (Fig. 2E). 3D data made it appealing to use micro-CT to measure bone-implant contact, but limited correlation with histological results has been reported and attributed to metal-induced artifacts that compromise the accuracy of the first few voxels at the interface (Palmquist et al., 2017).

Micro-CT also visualizes the internal microarchitecture of bone in 3D, aiding in the analysis of vasculature, porosity, and remodeling. Intracortical porosity, exemplified by the network of blood vessels within bone, is a key indicator of bone strength and quality, where increased porosity is linked to bone fragility and osteoporosis. The morphology of basic multicellular units during bone remodeling provides insights into bone diseases and the effectiveness of treatments (Loundagin and Cooper, 2022). On the other hand, soft tissues such as ligaments and tendons lack sufficient contrast for clear imaging due to their inherently low X-ray attenuation. Chemical agents such as phosphotungstic acid (and others, e.g., iodine, phosphomolybdic acid) allow visualization of intricate structures such as the Achilles tendon by selectively staining tissues and enhancing the contrast during scanning (Sartori et al., 2018).

2.3. *X-ray scattering: WAXS and SAXS*

X-rays have been widely employed not only for 3D imaging of bone via tomography, but also to gain structural information indirectly via X-ray scattering. The two main techniques used for this purpose, often performed simultaneously, are wide-angle X-ray scattering (WAXS) and small-angle X-ray scattering (SAXS). In these experiments, an X-ray micro-beam hits the sample and is scattered upon passing through it. Beam size ranges from 100 to 200 μm in laboratory settings, down to 1–10 μm at synchrotron radiation facilities, while the sample thickness is ideally matched to the beam size (Paris, 2008). The scattered photons are collected by a detector to retrieve 2D diffraction (scattering) patterns, which can also be acquired over an area of the sample by scanning the beam with a step size close to the beam size. WAXS patterns of polycrystalline samples (like bone) are made of arcs/rings, e.g., (002) planes of hydroxy(l)apatite, corresponding to the crystallographic planes diffracting according to Bragg's law, while SAXS focuses on the angular region around the beam tail (0.1–1°) (Guagliardi et al., 2009). WAXS can provide information on the crystal structure and texture, for example by mapping the orientation of collagen fibrils in bone using the *c*-axis of the mineral (Paris, 2008). This has been applied in combination with SAXS to examine the organization of mineralized collagen fibrils within individual lamellae in osteonal bone, to demonstrate helicoidal (spiral) winding around the Haversian canal (Wagermaier et al., 2006). SAXS alone has been widely employed to determine the size, shape, and orientation of mineral platelets in bone (Fratzl et al., 1996). More advanced applications of SAXS/WAXS include tensor tomography (Georgiadis et al., 2016), which has been recently used to map in 3D the orientation of mineral crystallites as a function of the distance from the Haversian canal (Grünewald et al., 2023).

3. Retrieving compositional information via vibrational spectroscopy

Two complementary techniques, FTIR and Raman spectroscopy, have been utilized extensively in the investigation of bone quality (Taylor and Donnelly, 2020; Boskey and Mendelsohn, 2005a; Morris and Mandair, 2011), i.e., the relationship between bone material properties and mechanical strength. An emerging technique called optical photothermal IR spectroscopy (O-PTIR) allows simultaneous IR and Raman spectroscopic analyses at the sub-micrometer level (Rahmati et al., 2022; Reiner et al., 2023). The underlying principle of both techniques is the transition between vibrational energy states of molecules. Infrared (IR) transitions arise directly from absorption of energy in the infrared range, whereas Raman spectra arise from the scattering of photons (in the visible or ultraviolet range) that have lost or gained part of their energy upon interaction with vibrating bonds. Every molecule exhibits distinctive vibrational characteristics leading to unique IR and Raman spectral signatures. The position, intensity, and width of a vibrational band reveal information that enables identification of specific functional groups or regions within a chemical species. Some vibrations are only IR active or Raman active, therefore the IR and Raman spectra of a given sample differ considerably but provide complimentary information (Taylor and Donnelly, 2020). Spectrometers are coupled with optical microscopes in modern instruments, hence the term micro-spectroscopy. By acquiring spectra over consecutive points in specific area of the sample, specific spectral features (e.g., peak intensity or area ratios between different bands) can be extracted to obtain a map of their spatial distribution (hyperspectral mapping). The compositional parameters commonly investigated include the mineral-to-matrix ratio, carbonate-to-phosphate ratio, mineral crystallinity (also referred to as “mineral maturity”), collagen cross-linking, and organic components such as proteoglycans and lipids (Fig. 3A).

3.1. Mineral-to-matrix ratio

The mineral-to-matrix ratio represents the amount of mineral with respect to the organic matrix. Since the mechanical properties of bone tissue are contingent upon both the mineral and organic matrix components, it is essential to factor in the organic matrix content (Martin and Ishida, 1989). In FTIR spectroscopy, the mineral-to-matrix ratio is determined as the ratio of the integral areas of the ν_1, ν_3 PO_4^{3-} to amide I band (C═O stretching) or amide II band (N—H bending and C—N stretching). Similarly, in Raman spectroscopy, the mineral-to-matrix ratio is taken as either the ratio between the integral areas of ν_1 or ν_2

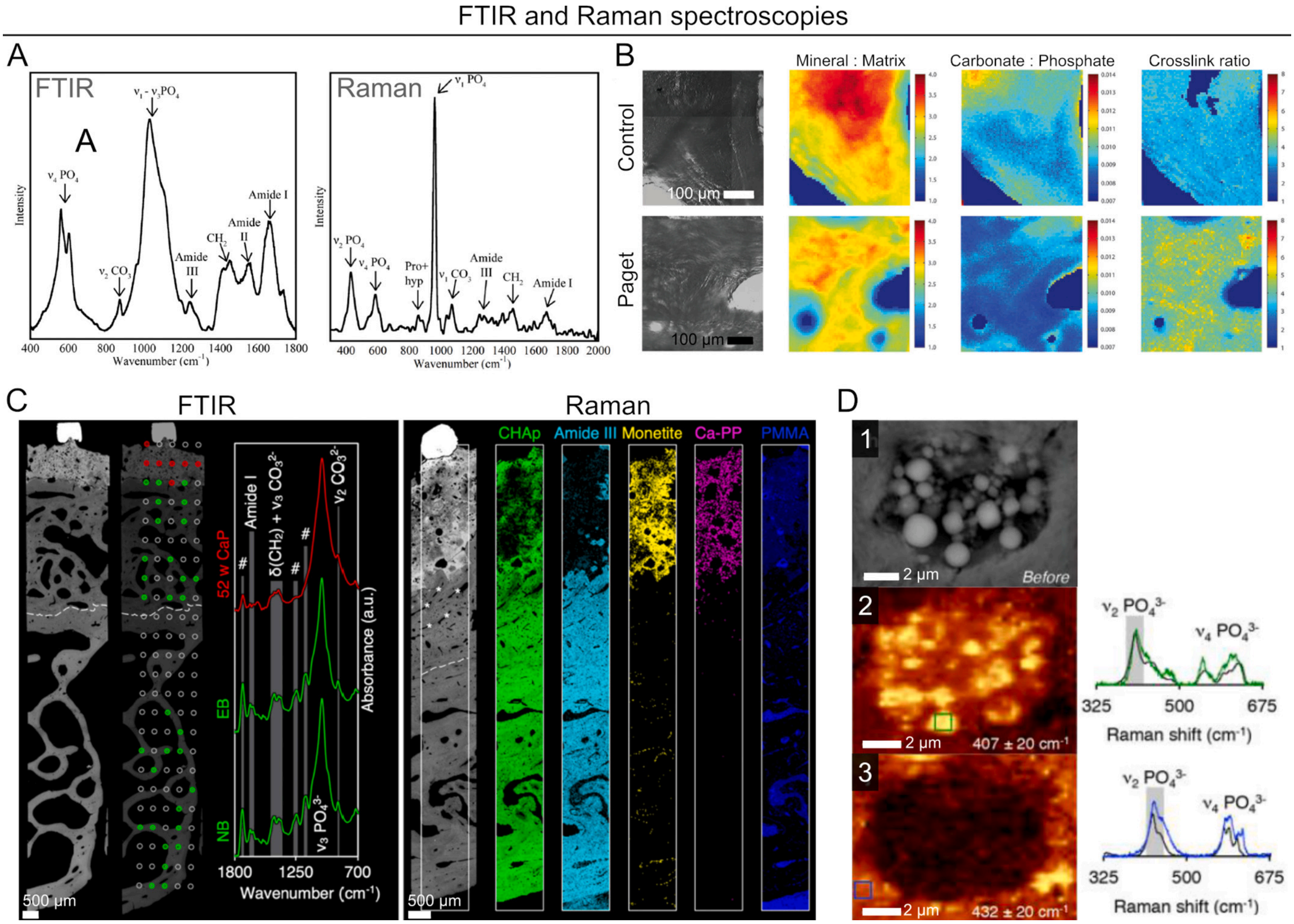

Fig. 3. Compositional analyses with vibrational spectroscopy. A) Typical FTIR (left) and Raman (right) spectra of bone [adapted from Taylor and Donnelly (2020) with permission, Copyright 2020, Elsevier]. B) FTIR maps of various metrics related to bone quality (mineral-to-matrix ratio, carbonate-to-phosphate ratio, and collagen cross-link ratio) in healthy conditions (top row) and in presence of Paget's disease (bottom row) [adapted from Zimmermann et al. (2015) with permission, Copyright 2014, John Wiley & Sons]. C) FTIR spectra (left) and Raman maps (right) acquired at the interface between bone and a calcium phosphate-based biomaterial [adapted from Shah et al. (2022) with permission, Copyright 2022, Elsevier]. D) BSE-SEM image (panel 1) and Raman maps of the ν_2 PO_4^{3-} band showing whitlockite (panel 2) and carbonated apatite (panel 3) in an osteocyte lacuna with micropetrosis in an individual treated with anti-resorptive agents [adapted from Shah et al. (2017) with permission, Copyright 2017, American Chemical Society].

PO_4^{3-} to either amide I or amide III, with consideration to polarization effects since both ν_1 PO_4^{3-} and amide I bands are sensitive to sample orientation (Kazanci et al., 2006a; Gamsjaeger et al., 2010). Due to the orientation sensitivity of the amide I band, alternatives such as the proline (~853 cm^{-1}), hydroxyproline (~876 cm^{-1}), or phenylalanine (~1001 cm^{-1}) bands may be used as markers for the organic phase. The mineral-to-matrix ratio computed as ν_1 PO_4^{3-}/phenylalanine has been used to track mineral accumulation over time in calvarial tissue cultures (McElderry et al., 2013) or to determine the degree of mineralization in bisphosphonate-exposed necrotic bone (Micheletti et al., 2022b). The mineral-to-matrix ratio tends to correlate with ash weight measurements in healthy bone (Boskey and Mendelsohn, 2005b), has been shown to be proportional to several mechanical properties (e.g., bending stiffness and failure moment), and is a more accurate predictor of bending stiffness than bone mineral density (Donnelly et al., 2010). The mineral-to-matrix ratio is also sensitive to various physiological conditions. For example, it increases with increasing tissue age in healthy individuals (Gamsjaeger et al., 2014a) and decreases in osteoporosis (Boskey et al., 2005). Variations in mineral-to-matrix ratio can also be used to assess mineralization heterogeneity as observed in pathological conditions, such as Paget's disease (Zimmermann et al., 2015) (Fig. 3B).

3.2. *Carbonate substitution and mineral crystallinity*

Both FTIR and Raman spectroscopy reveal information on the chemical nature of bone mineral crystallites and impurities such as carbonate ions (Taylor et al., 2021; Shah, 2020), and their shape and/or size (Gadaleta et al., 1996; Kazanci et al., 2006b; M. Wang et al., 2018). In the apatite lattice, substitution of phosphate groups by carbonate ions increases with tissue age. The extent of this substitution is evaluated by FTIR and Raman spectroscopy as the ratio between the integral areas of the carbonate band (ν_2 CO_3^{2-} in FTIR and ν_1 CO_3^{2-} in Raman spectroscopy) to the phosphate band (Boskey and Mendelsohn, 2005a; Morris and Mandair, 2011).

Mineral crystallinity is a hybrid measure of crystallite size (e.g., length along the crystallographic *c*-axis) and stoichiometric perfection, which is affected by carbonate substitution, and not strictly a measure of crystalline/amorphous nature of the material (Yerramshetty and Akkus, 2008). In FTIR spectroscopy, the most common method for deriving mineral crystallinity involves deconvolution of the underlying peaks in the ν_1, ν_3 PO_4^{3-} region using methods such as second derivative spectroscopy (Paschalis et al., 1996; Spevak et al., 2013). In Raman spectroscopy, mineral crystallinity is obtained as the inverse full-width at half maximum (1/FWHM) of the ν_1 PO_4^{3-} band centered at ~960 cm^{-1} (Morris and Mandair, 2011). The contribution of mineral crystallinity to bone strength is substantiated by the fact that osteoporotic bone exhibits mineral of higher crystallinity than healthy bone (Boskey et al., 2005; Paschalis et al., 1996, 1997; Huang et al., 2003).

3.3. *Collagen cross-linking*

Molecular packing and cross-linking chemistry are a distinct feature of type I collagen in mineralized tissues (Knott and Bailey, 1998). The density of collagen intermolecular cross-links poses a direct impact on the mechanical performance of bone (Oxlund et al., 1995). Two types of the collagen cross-links, (i) pyridinoline (PYD) trivalent collagen cross-links and (ii) divalent cross-links can be quantified using FTIR and Raman spectroscopy (Morris and Mandair, 2011; Gamsjaeger et al., 2014a; Carden et al., 2003; Fratzl et al., 2004). This can be achieved through deconvolution of sub-bands underlying the amide I region, particularly the spectral component at 1660 cm^{-1}, by second derivative spectroscopy (Paschalis et al., 2001). Several FTIR-based investigations have shown that the ratio of PYD to divalent cross-links strongly correlates with the incidence of fracture (Gourion-Arsiquaud et al., 2009; Paschalis et al., 2004, 2005; Blank et al., 2003), attesting to the relationship between collagen cross-linking and bone quality (Paschalis et al., 2011). The possibility to accurately monitor PYD content has been validated through the application of high-performance liquid chromatography (HPLC) on bone and collagenous tissues (McNerny et al., 2015; Gamsjaeger et al., 2017). It should be noted that the Raman 1660/1690 cm^{-1} ratio may be influenced by features of collagen secondary structure.

3.4. *Proteoglycans and lipids*

In bone, proteoglycans are implicated in various roles, influencing mineralization of the organic matrix and rates of bone remodeling, while lipids have been identified as initiators of collagen mineralization (Boskey and Reddi, 1983; Goldberg and Boskey, 1996) and implicated in the accumulation of advanced glycation end-products (AGEs) (Ramasamy et al., 2005), which is associated with higher risk of bone fracture (Tang et al., 2007). In bone and other mineralized tissues, the characteristic FTIR spectral band for proteoglycans (around 1060 cm^{-1}) is overlapped by the ν_3 PO_4^{3-} band. In contrast, proteoglycans can be detected by Raman spectroscopy, where a band around1375 cm^{-1} is assigned as CH_3 symmetric deformation of glycosaminoglycan (GAG) groups (Gamsjaeger et al., 2011, 2014b). The spatial distribution of lipids can be mapped using Raman spectroscopy, where spectral features around ~1060 cm^{-1}, ~1079 cm^{-1}, ~1300 cm^{-1}, ~1439 cm^{-1}, and ~1745 cm^{-1} are indicative of tissue lipids (Frushour and Koenig, 1975; Penel et al., 2005). The band at ~1300 cm^{-1} is attributed to methylene twisting vibrations and is particularly valuable since it does not overlap any of the collagen bands (Frushour and Koenig, 1975). The ratio of the integrated area of this band normalized to the integrated area of the amide III band can be employed to characterize the relative lipid content in mineralized tissues (Gamsjaeger et al., 2014a).

3.5. *Bone around implant biomaterials*

All the bone quality metrics described above can also be evaluated in bone formed around implant biomaterials, making FTIR and Raman spectroscopy valuable tools in understanding bone-biomaterial interactions. For example, Raman spectroscopy has been used together with techniques, such as BSE-SEM imaging and histology, to evaluate the response of bone response to different types of implant designs, e.g., machined vs. laser-modified micro- and nano-rough surface (Shah et al., 2016a), solid vs. porous design by 3D printing (Shah et al., 2016b), or Ti alloy-based vs. CoCr-based (Shah et al., 2016c). Applications are not limited to metallic implants, but also encompass bone formation around calcium phosphate biomaterials, where examples include intra-vital Raman spectroscopy (Penel et al., 2005), FTIR mapping (Bohner et al., 2017), or complementary approaches combining both FTIR and Raman spectroscopy (Shah et al., 2022) (Fig. 3C).

3.6. *Detection of rare calcium phosphate phases in bone*

Other uses of these vibrational spectroscopy are aimed at identifying the composition of specific features, such as mineral nodules formed within osteocyte lacunae in micropetrosis in elderly individuals (Milovanovic et al., 2017) or following treatments with anti-resorptive medications, where discrete crystals of magnesium whitlockite have been identified (Shah et al., 2017; Shah, 2023) (Fig. 3D). The effects of anti-resorptive agents on bone quality have also been examined with Raman spectroscopy, where the presence of pyrophosphate in bone chips from atypical femoral fractures offers a potential explanation for the reduced bone strength (Shabestari et al., 2017).

4. Probing structure and composition with electrons

4.1. *SEM: structural information with BSE and SE*

SEM has found extensive application in characterization of bone

(Shah et al., 2019b), since common features in bone microscale architecture, such as osteons with their concentric lamellae, and cellular components such as osteocyte lacunae, can be readily resolved in SEM images with greater resolution than light microscopy, down to 1–10 nm in modern SEM instruments. In the SEM, an electron beam is focused onto the surface of the sample and scanned over a squared/rectangular area one point (pixel) at a time. The interaction of the electron beam with the atoms in the sample generates various signals that can be collected by appropriate detectors to retrieve different types of information (Goldstein et al., 2018). SEM traditionally operates in high-vacuum conditions, although variable-pressure/environmental SEMs are also available. Imaging in low-vacuum removes the necessity of coating bone samples with conductive materials (e.g., C or Au), but limits the resolution at higher magnifications. Detailed information on bone sample preparation for SEM and experimental conditions are reviewed by Boyde (Boyde, 2019).

In bone imaging, electrons elastically scattered "backwards" and out from the sample surface (backscattered electrons, BSEs) are widely employed because of the ease of the interpretation of the resulting images, where contrast mostly depends on the atomic number (thus referred to as compositional or Z-contrast) (Goldstein et al., 2018). In this manner, different materials can be clearly recognized, for example, bone vs. metal biomaterial in the peri-implant space. Mineralization heterogeneities are also captured in BSE mode, with more mineralized areas appearing brighter due to an increased average Z (Fig. 4A).

Alternatively, SEM images can be also created using secondary electrons (SEs). SEs are generated from the first few tens of nanometers below the sample surface, hence the SE signal is mostly affected by surface topography (Goldstein et al., 2018). While SE-SEM is of little use for imaging embedded and polished bone surfaces, it is the imaging mode of choice when inspecting bone samples rich in topographical cues, for example after treatments such as acid etching to reveal the

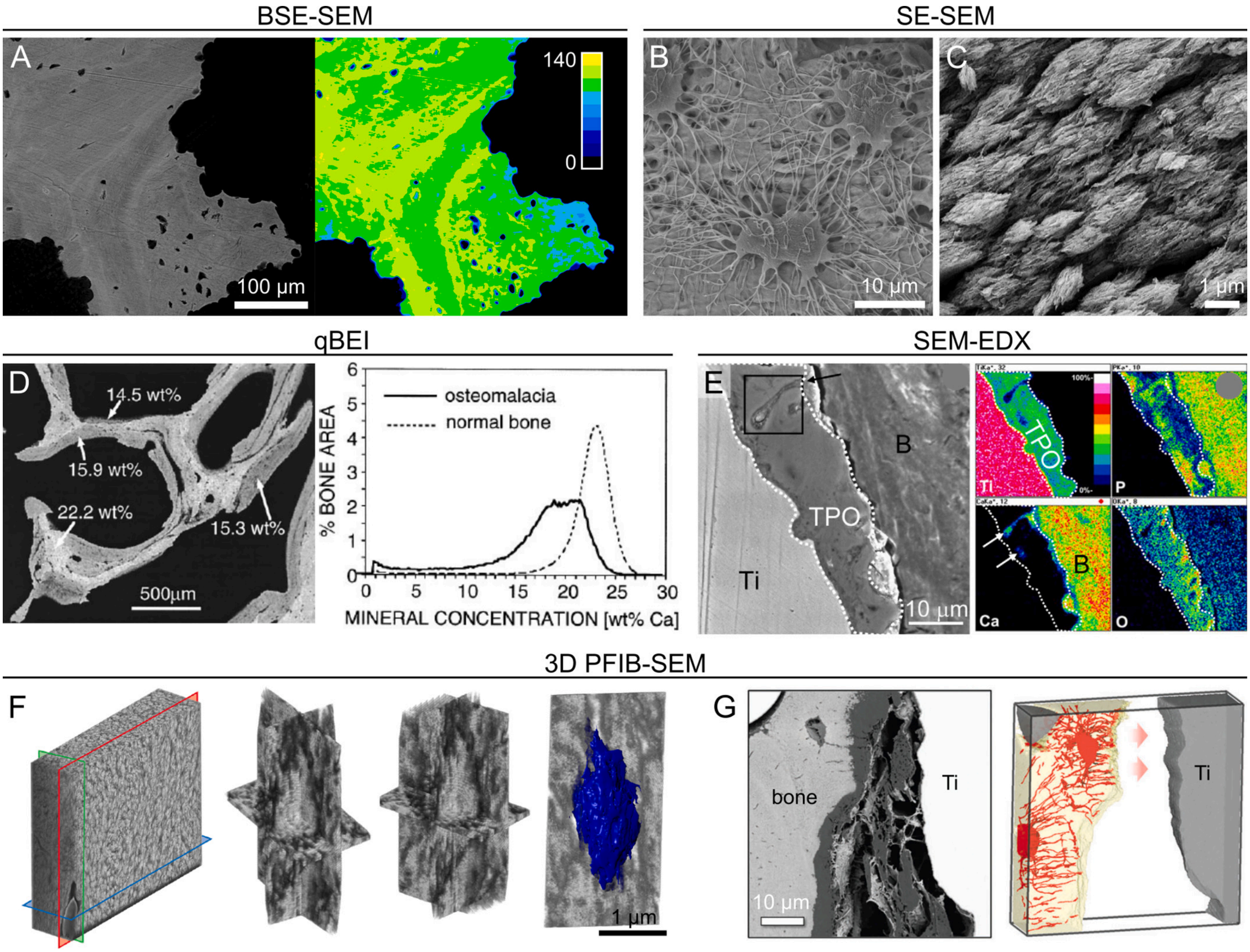

Fig. 4. SEM-based structural and compositional characterization. A) BSE-SEM image of necrotic bone following anti-resorptive treatment showing areas with heterogeneous mineralization, more apparent in the false-colored version on the right [adapted from Micheletti et al. (2022b) with permission, Copyright 2022, CC-BY License]. B) SE-SEM image of the LCN after resin cast etching [unpublished]. C) SE-SEM image of marquise-shaped mineral aggregates after deproteinization [adapted from Shah et al. (2020) with permission, Copyright 2020, CC-BY License]. D) qBEI analysis of bone from a patient affected by osteomalacia where grey-levels have been converted into mineral density (left image) and corresponding bone mineral density distribution histogram where a comparison with normal bone is provided (right plot) [adapted from Roschger et al. (1998) with permission, Copyright 1998, Elsevier]. E) SEM image (left) of the interface between bone ("B" label) and implant ("Ti" label) with a porous oxide coating ("TPO" label) and EDX maps (right) for Ti, P, Ca, and O corresponding to the area marked by the square on the SEM image [adapted from Wierzchos et al. (2008) with permission, Copyright 2008, Elsevier]. F) PFIB-SEM reconstruction of a section of human femur from which representative cross-sectional views of a mineral ellipsoid (or tesselle) are extracted (the 3D rendering of the mineral ellipsoid is shown in blue) [adapted from Binkley et al. (2020) with permission, Copyright 2020, Elsevier]. G) 2D slice (left) and 3D reconstruction (right) of the bone-implant interface from PFIB-SEM tomography (segmented LCN is shown in red in the 3D reconstruction) [adapted from Deering et al. (2023) with permission, Copyright 2023, CC-BY License].

resin-infiltrated LCN (Sato and Shah, 2023) (Fig. 4B), or deproteinization, where mineral organization at the osteocyte lacuna floor (Shah et al., 2016d) or marquise-shaped mineral agglomerates (Shah et al., 2020) can be imaged (Fig. 4C).

4.2. *SEM: compositional information with quantitative BSE imaging and X-rays*

Z-contrast in BSE-SEM offers indirect compositional information, although individual elements cannot be identified nor quantified. However, a technique now commonly called "quantitative backscattered electron imaging" (qBEI) has been developed to convert pixel intensity (grey-level) into mineral content (Boyde et al., 1992; Roschger et al., 1998). This technique is based on the calibration of pixel intensity using standards usually made of carbon and aluminum to have a linear relationship between grey-levels and Z, which can be used to convert the grey-levels of calibrated BSE-SEM images into calcium content (wt% Ca). The wt% Ca histogram extracted from qBEI images can be used to compute various metrics describing the bone mineral density distribution, as detailed by Roschger et al. (Roschger et al., 1998) (Fig. 4D).

While qBEI can provide insights on mineralization levels in bone, precise determination of composition, also extended to non-bone regions in the sample, e.g., when dealing with bone-implant interfaces, can be obtained with energy-dispersive X-ray spectroscopy (EDX). EDX is based on the detection of characteristic, i.e., element-specific, X-rays emitted from the sample following electron beam excitation (Goldstein et al., 2018). This makes it possible to determine elemental composition in specific points of the sample surface, along lines across interfaces or other regions of interest, or across entire areas. Elemental analysis in SEM is routinely used to assess bone mineralization, for example quantifying Ca and P and evaluating their ratio (Ca/P) (Åkesson et al., 1994), or to obtain compositional information at the bone-implant interface (Wierzchos et al., 2008; Palmquist et al., 2010) (Fig. 4E).

4.3. *Extending SEM in 3D: FIB-SEM tomography*

Despite a good depth of field/focus that yields 3D-like images, SEM is limited to 2D information from the sample surface. Combining SEM with a FIB in dual-beam instruments makes it possible to expand SEM imaging in 3D. Specifically, in FIB-SEM tomography (also referred to as "serial surface view", "serial slice-and-view", and "serial sectioning"), cross-sections of material are progressively exposed by milling with the ion beam and subsequently imaged with the electron beam. The so-generated stack of SEM images (typically BSE for examining mineralized tissues) is then aligned to generate a 3D reconstruction of the volume of material (Weiner et al., 2021; Uchic et al., 2007; Cantoni and Holzer, 2014).

Applications of FIB-SEM tomography in bone biology have focused quite extensively on determining collagen fibril organization in lamellar bone (Faingold et al., 2013; Reznikov et al., 2014b, 2013). The combination of 3D imaging with nanoscale resolution (down to 5–10 nm in terms of slice thickness) offers various advantages compared to other techniques used for this purpose, such as light microscopy (lower resolution, 2D), SAXS (no direct structural visualization, but indirect information on orientation only), and SEM (2D). While early work on collagen fibril orientation was mostly limited to demineralized bone stained to enhance fibril contrast (e.g., following the OTOTO protocol (Reznikov et al., 2013)), this characterization technique has also been expanded to mineralized bone (Binkley et al., 2020; Raguin et al., 2021). In particular, FIB-SEM tomography of mineralized bone has informed new perspectives on the mesoscale organization of bone mineral, revealing tessellated patterns of mineral ellipsoids/tesselles in both mouse (Buss et al., 2020) and human bone (Binkley et al., 2020) (Fig. 4F). The applications of FIB-SEM tomography are not limited to studying the organization of collagen fibrils and mineral in the extracellular matrix. Noteworthy examples include visualization and quantitative analyses of the LCN (Schneider et al., 2011), and more recently, of a system of interconnected "nanochannels", postulated to provide an additional system to canaliculi in ion transportation (Tang et al., 2022, 2023).

In biomaterials science, FIB-SEM tomography can provide higher-resolution information on bone-implant contact compared to micro-CT, for example, better resolving bone growth within specific features of surface-modified micro-rough implants (Giannuzzi et al., 2005). The potential of FIB-SEM tomography in this area can be further expanded by Xe^+ plasma (plasma FIB, PFIB) dual beam instruments, as already demonstrated for native bone (Binkley et al., 2020). Compared to conventional Ga^+ ion beams, Xe^+ mills at higher rates, making it possible to examine larger volumes of material (Burnett et al., 2016), in this case of peri-implant bone. Recent applications of PFIB-SEM tomography exemplified how this technique is suited not just to evaluate the bone-implant interface, but also the mesoscale structure of peri-implant bone, and specifically of mineral ellipsoids/tesselles and the LCN (Deering et al., 2023) (Fig. 4G).

4.4. *S/TEM: imaging and electron diffraction*

An even higher resolution, down to sub-nanometer scale, can be achieved with transmission electron microscopy (TEM). In conventional, i.e., parallel beam, TEM, the electron beam illuminates an area over an ultrathin sample, generating various signals as it interacts with the atoms in the sample (Williams and Carter, 2009). Limited thickness ensures electron transparency, where bone samples are typically less than 300 nm thick (Binkley and Grandfield, 2017), but maintaining structural integrity is challenging for thinner samples. However, samples up to 700 nm in thickness have also been successfully examined (Micheletti et al., 2023). The transmitted, undeviated electron beam can be collected to generate bright field (BF) images, where the contrast depends on diffraction and mass/thickness variations in the sample (Williams and Carter, 2009). BF is the imaging mode originally available in TEM instruments, and hence has been used in the very early studies on tropocollagen self-assembly (Hodge and Petruska, 1963), and bone mineral shape and size (Robinson, 1952), and the spatial distribution of non-collagenous proteins such as osteopontin and osteocalcin through immunolocalization methods (McKee et al., 1993), including in the vicinity of bone anchored implants (Ayukawa et al., 1998). TEM has also been fundamental in studying the bone-implant interface, revealing that osseointegration occurs at the nanoscale, at the "electron microscopic level" surpassing the "light microscopic level" (Albrektsson et al., 1981).

TEM instruments are now also commonly equipped with a scanning mode, i.e., scanning TEM (STEM). In STEM, the electron beam is not parallel any longer, but is made convergent and scanned across the sample point by point, similarly to SEM (Carter and Williams, 2016). Combined with annular dark-field detectors, STEM makes it possible to obtain images from electrons scattered at higher angles than in BF-TEM. Particularly, high-angle annular dark-field (HAADF)-STEM is now extensively used for resolving bone and bone-implant interfaces at the nanoscale. In HAADF-STEM, the electrons used to form images are those incoherently scattered at high angles (Rutherford scattering). As a result, the pixel intensity is roughly proportional to Z^2 (Z-contrast), and the overall image contrast is related to mass/thickness variations, removing diffraction-contrast contributions (Pennycook, 1989).

Both BF-TEM and HAADF-STEM, together with electron tomography (discussed later), have been largely used to investigate the ultrastructural organization of bone, specifically the collagen-mineral spatial relationship (McNally et al., 2012; Weiner and Traub, 1986; Cressey and Cressey, 2003; Arsenault, 1989), starting with the pioneering work of Robinson (Robinson, 1952). Note that the collagen-mineral organization is sometimes studied in mineralized turkey tendon as a model for *bone*, where *bone* refers to a family of tissues other than the skeletal one built upon mineralized collagen fibrils (Weiner and Wagner, 1998). S/TEM imaging has revealed different organizational motifs have been identified based on whether collagen fibrils are in-plane (longitudinal or filamentous motif) or out-of-plane (lacy motif), i.e., oriented parallel or perpendicular to the image plane, respectively (McNally et al., 2012; Grandfield et al., 2018; Reznikov et al., 2018; Jantou et al., 2009) (Fig. 5A). An important advancement in S/TEM studies of bone ultrastructure and bone-biomaterial interfaces was enabled by the use of FIB (Giannuzzi et al., 2005; Jarmar et al., 2008), to prepare electron transparent samples in a highly site-specific manner, at the same time preserving greater structural integrity compared to other techniques such as ultramicrotomy (Jantou et al., 2009; Grandfield and Engqvist, 2012).

Information on crystal structure can also be obtained in S/TEM through electron diffraction. Typically, an aperture is used to collect diffraction patterns restrictively from a specific region of the sample (selected area electron diffraction, SAED). Electron diffraction studies of mineralized collagen fibrils have confirmed that the longest dimension of bone mineral crystallites (i.e., the crystallographic *c*-axis) is co-aligned with the collagen fibrils (Traub et al., 1989) (Fig. 5B).

In an additional imaging mode, dark-field (DF)-TEM, electrons scattered at specific angles can be selected by positioning the objective aperture on specific spots in the diffraction pattern, in turn creating images where only the features meeting the selected diffraction conditions are illuminated (Williams and Carter, 2009). DF-TEM has been used in conjunction with BF-TEM to examine collagen-mineral spatial relationship, especially providing crystallographic/structural information on intra- vs. extrafibrillar mineralization (Arsenault, 1989; Schwarcz et al., 2014, 2020) (Fig. 5C). Alternatively, information regarding crystal structure can be retrieved by applying a fast Fourier transform (FFT) operation to high resolution TEM (HRTEM) images, a strategy that has been used to confirm the presence of crystalline apatite-like mineral in bone juxtaposed to the implant (Palmquist et al., 2010; Grandfield et al., 2013a).

4.5. Extending S/TEM in 3D: electron tomography

Despite S/TEM offering unrivaled resolution of bone structure at the (sub)nanoscale, images are 2D projections where all features along the sample thickness overlap onto the same image plane. For example, the 2D nature of TEM images has led to controversy regarding the shape of bone mineral, as edge-on views of plates can be interpreted as needles/rods (Bocciarelli, 1970). 3D imaging in TEM can be achieved with electron tomography. This consists in acquiring images at different tilt angles, usually with small increment steps such as 2°, aligning them with fiducials or by cross-correlation, and reconstructing them into a 3D volume using specialized algorithms like the simultaneous iterative reconstruction technique (SIRT) (Bals et al., 2013; Ercius et al., 2015). As mentioned earlier, this technique has been extensively applied in ultrastructural studies, exploiting the three-dimensionality to better resolve collagen-mineral organization (Landis et al., 1993, 1996a, 1996b; Reznikov et al., 2018; Landis and Song, 1991; McNally et al., 2013), as well as bone-biomaterial interfaces for a wide range of implant materials, from metals (Grandfield et al., 2013a, 2013b; Palmquist et al., 2012a; Thorfve et al., 2014; Shah et al., 2015a) to ceramics (Grandfield et al., 2010; Micheletti et al., 2021) (Fig. 5D). While earlier studies used high-voltage TEM instruments (Landis et al., 1993, 1996a, 1996b; Landis and Song, 1991), HAADF-STEM electron tomography, also called Z-contrast electron tomography, is now the preferred choice for bone studies (Micheletti et al., 2023; Reznikov et al., 2018; McNally et al., 2013). STEM electron tomography in fact better fulfills the so-called "projection theorem" dictating image intensity requirement in electron tomography, which is instead violated in BF-TEM due to the diffraction contrast arising from the crystalline nature of bone mineral (Grandfield et al., 2012). Alternatively, electron tomography can also be completed in cryogenic mode, for example to study collagen mineralization in close-to-native conditions (Nudelman et al., 2010).

Typically, the tilt range in electron tomography experiments is limited to ±70° due to shadowing from the sample holder. This results in a "missing wedge"-shaped region of unsampled information where no images are collected, degrading the quality of the final reconstruction, and introducing distortions (Bals et al., 2013; Ercius et al., 2015). Rotation tomography holder and rod-shaped samples allow for acquisition over the entire ±90° range, eliminating missing wedge artifacts (Kawase et al., 2007). This technique, termed on-axis electron tomography, has been successfully applied to rod-shaped samples of bone-titanium prepared by FIB (Huang et al., 2014), demonstrating higher fidelity reconstructions than conventional electron tomography (Wang et al., 2017). More recently, we applied on-axis Z-contrast electron tomography to the study of human bone ultrastructure, demonstrating the collagenous nature of long-debated nanosized pores in bone and the platelet-like habit of bone mineral (Micheletti et al., 2023) (Fig. 5E).

4.6. Analytical S/TEM and spectroscopic tomographies

Signals generated by the interaction of the electron beam with the sample also carry compositional information, making TEM also an analytical tool where structural information from images can be correlated with composition. All the nano-analytical techniques described in this section can be coupled with a tomography acquisition scheme to gain compositional information in 3D (Midgley and Weyland, 2003; Collins and Midgley, 2017). This can be correlated with the structural information retrieved by Z-contrast electron tomography, leading to 4D characterization at the nanoscale, where the 4th dimension refers to the spectroscopic data.

As in the SEM, characteristic X-rays can be produced when the incident TEM electron beam causes the emission of inner shell electrons in the sample (Williams and Carter, 2009). When EDX is combined with STEM, elemental analysis can be performed at specific points of the TEM sample or mapped over entire areas. Therefore, 2D STEM-EDX has been used extensively for examining bone, for example, to quantify intra- vs. extra-fibrillar mineral, highlighting higher Ca and P signals for the latter (McNally et al., 2012), a trend also confirmed in 3D through on-axis EDX tomography (Micheletti et al., 2023) (Fig. 5F).

The transmitted electrons themselves can be used to obtain compositional information. In energy-filtered TEM (EFTEM), energy filters are used to select electrons scattered with specific energies, so that the final image is created only by those electrons (Verbeeck et al., 2004). In particular, by filtering according to element-specific ionization energies, elemental distribution maps (i.e., electron spectroscopic images) with nanoscale resolution can be obtained, for example, to determine the distribution of Ca and P at early mineralization sites (Arsenault and Ottensmeyer, 1983; Hoshi et al., 2001) (Fig. 5G). Loss of energy due to inelastic scattering events is also at the basis of electron energy-loss spectroscopy (EELS). In EELS, a convergent electron beam (STEM mode) is scanned over a region of interest and the energy-loss spectrum is recorded at each position of the probe (Egerton, 2011). Of the three regions in a typical EELS spectrum, i.e., zero-loss (elastically scattered electrons), low-loss (plasmon peaks), and high-loss (core ionization edges), the last one is particularly valuable for obtaining compositional information from bone. The peaks in the high-loss region correspond to scattering events with core electrons, hence they can be used to identify and quantify the elements present and map their distribution. EELS affords higher spatial resolution and chemical sensitivity than EDX (Titchmarsh, 1989), but it is more stringent in terms of sample thickness, which needs to be as thin as possible to maximize collection of electrons transmitted through the sample, hence better signal quality. In bone ultrastructure studies, Alexander et al. have employed EELS to probe the main location of the mineral with respect to gap and overlap zones of the collagen fibrils (Alexander et al., 2012) (Fig. 5H). EELS has also contributed to the debate on the nature of the "holes" within the lacy pattern, supporting that they correspond to collagen fibrils in cross-section in both bone (Lee et al., 2019) and dentin (Jantou-Morris et al., 2010). In bone pathology, EELS maps, in conjunction with EDX and Raman spectroscopy, have revealed fundamental information on the

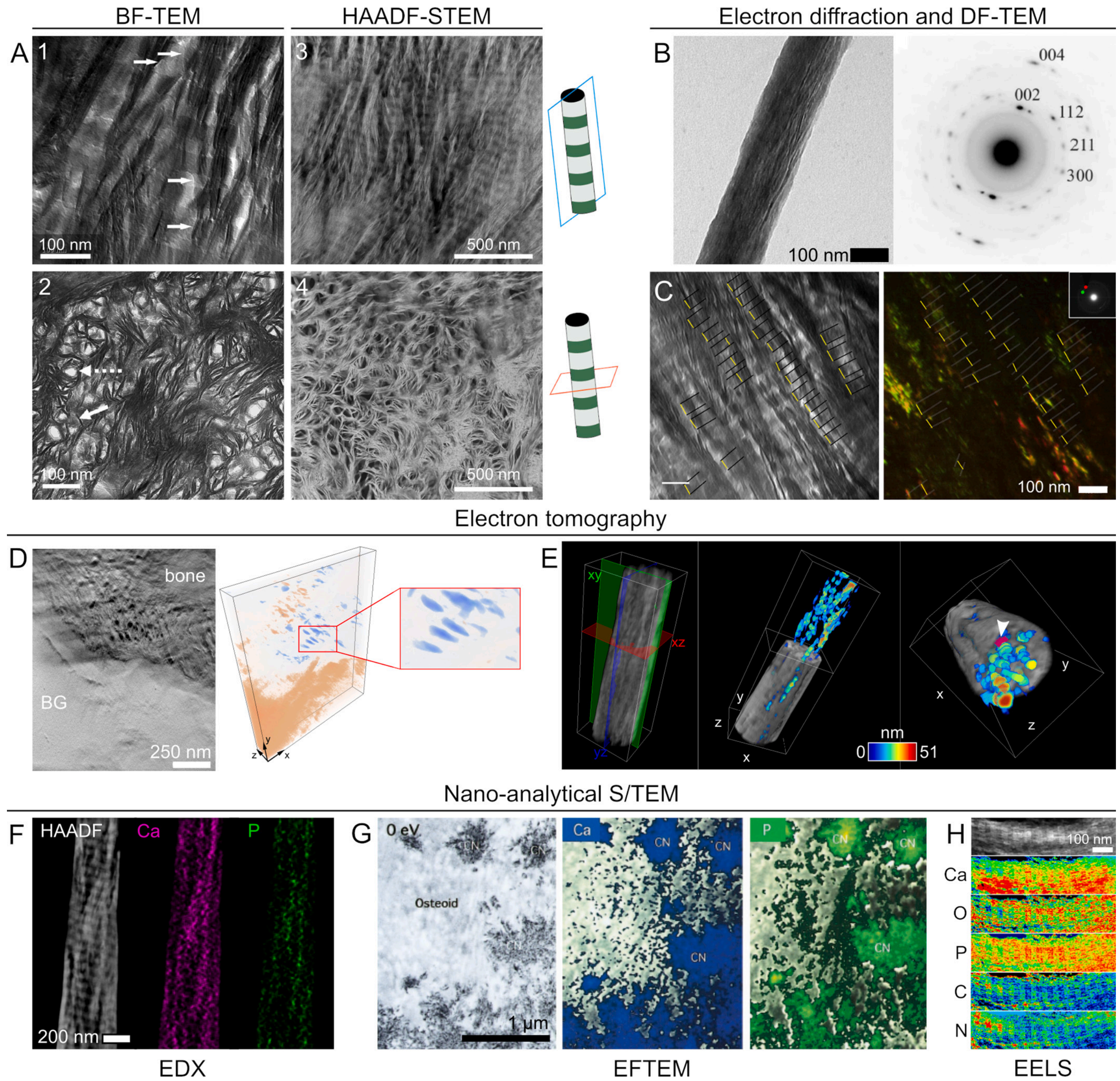

Fig. 5. Nanoscale structural and compositional information with S/TEM. A) Typical BF-TEM and HAADF-STEM images of the longitudinal (panels 1 and 2) and lacy (panels 3 and 4 with magnified inset) motifs corresponding to in-plane and out-of-plane views of mineralized collagen fibrils, respectively [A-1: adapted from McNally et al. (2012) with permission, Copyright 2012, McNally et al.; A-2: adapted from Schwarcz et al. (2014) with permission, Copyright 2014, Elsevier; A-3,4: adapted from Micheletti et al. (2023) (see Supporting information) with permission, Copyright 2023, American Chemical Society, CC-BY 4.0 License]. B) BF-TEM image (left) and corresponding electron diffraction pattern (right) with the characteristic (002) arcs indicative of the *c*-axis of bone mineral [adapted from Deshpande and Beniash (2008) with permission, Copyright 2008, American Chemical Society]. C) BF-TEM image (left) and corresponding DF-TEM images (right, shown in red and green) obtained selecting two spots on the (002) (top right corner) [adapted from Schwarcz et al. (2020) with permission, Copyright 2020, Elsevier]. D) Electron tomography of the bone-bioactive glass ("BG" label) interface showing a 2D reconstructed slice (left) and the 3D volume (right) segmented to highlight collagen fibrils (blue) oriented parallel to the biomaterial surface (orange). The dimensions of the 3D volume are 1231 × 1494 × 161 nm^3 [adapted from Micheletti et al. (2021) with permission, Copyright 2021, The Royal Society]. E) On-axis electron tomography of human bone: reconstructed 3D volume (left) and segmentation of collagen fibrils (color-coded by size) and a representative mineral platelet (magenta, indicated by arrowhead on the right image). The dimensions of the 3D volume are 556 × 1611 × 457 nm^3 [adapted from Micheletti et al. (2023) with permission, Copyright 2023, American Chemical Society, CC-BY 4.0 License]. F) Reconstructed HAADF slice with corresponding EDX maps of Ca (magenta) and P (green) from correlative on-axis Z-contrast and EDX tomographies of human bone [adapted from Micheletti et al. (2023) with permission, Copyright 2023, American Chemical Society, CC-BY 4.0 License]. G) EFTEM of osteoid undergoing mineralization where calcified nodules ("CN" label) rich in Ca (blue map) and P (green map) are noted [adapted from Hoshi et al. (2001) with permission, Copyright 2021, John Wiley & Sons]. H) EELS maps of a mineralized collagen fibril (top image is the HAADF image) showing the distribution of Ca, O, P, C, and N (from lowest concentration in blue, to higher concentration in red) [adapted from Alexander et al. (2012) with permission, Copyright 2012, The Royal Society].

composition of mineral nodules detected in micropetrosis (mineralization of apoptotic osteocyte lacunae) of bisphosphonate-exposed bone (Shah et al., 2017).

The possibility to obtain spatially resolved compositional information at the nano-level has made the spectroscopic techniques described above suitable to probe elemental gradients at bone-biomaterial interfaces. Gradual intermixing of Ca and P (indicative of bone) with the oxide layer on the implant surface has been highlighted with EFTEM (Palmquist et al., 2010, 2009a; Grandfield et al., 2013a), STEM-EDX (Grandfield et al., 2013a; Budd et al., 1992; Shah et al., 2014), and STEM-EELS (Deering et al., 2023; Kim et al., 2015). In particular, EELS tomography demonstrated such elemental intermixing also in 3D (X. Wang et al., 2018a).

5. Simultaneously resolving structure and composition with mass spectrometry

Z-contrast electron tomography and spectroscopic tomography (EDX or EELS) have been successfully correlated to enable 4D characterization of bone and bone-biomaterial interfaces at the nanoscale (Micheletti et al., 2023; X. Wang et al., 2018a). Along similar lines, correlative characterization can be accomplished by mass spectrometry-based techniques.

Time-of-Flight Secondary Ion Mass Spectrometry (ToF-SIMS) enables high chemical sensitivity, allowing simultaneous analysis of both structure and composition. It operates by directing a focused, pulsed ion beam onto the surface of a sample, dislodging secondary ions (molecules or fragments) that are accelerated into a time-of-flight mass spectrometer, where their flight times are measured. The resulting mass spectrum reveals the mass-to-charge ratios (m/z) of the secondary ions, providing information about their elemental composition. Although ToF-SIMS is surface-sensitive, probing only the top few nanometers, depth profiling can be achieved by varying the primary ion energy to selectively sputter material from the sample surface (Fearn, 2015). ToF-SIMS has proven to be a valuable tool in the analysis of compositional changes in bone. Ca^+ and $C_4H_8N^+$ signals have been used to examine changes in bone mineral and collagen, respectively (Henss et al., 2013), whereas lipid distribution has been interpreted from the CN^- signal (Schaepe et al., 2018). The chemical and structural characteristics of the bone-implant interface have also been investigated using ToF-SIMS, offering valuable insights into the process of osseointegration of metal implants (Palmquist et al., 2012b), and phagocytosis of calcium phosphate biomaterials by macrophages (Malmberg et al., 2021).

Another tool to simultaneously retrieve structural and compositional information in 3D is APT, which achieves even higher spatial resolution (sub-nanoscale) and chemical sensitivity (down to ppm). APT combines field evaporation, accomplished with laser pulses for insulating materials like bone, with time-of-flight mass spectrometry to identify the evaporated ions. Data reconstruction consists of determining the position in the 3D space of each ionic species detected, which is identified from the recorded mass spectrum (Gault et al., 2021).

APT technique fundamentals (Gault et al., 2021) and applications of APT in bone and other mineralized tissues (Grandfield et al., 2022) are comprehensively reviewed elsewhere. Gordon et al. were the first to use APT to examine bone composition in a sample of rat cortical femur, highlighting the similarities with geological hydroxy(l)apatite with Mg and Na substitutions (Gordon et al., 2012) (Fig. 6A). Langelier et al. further expanded the study of bone using APT, correlating it with HAADF-STEM to identify the location of Ca (mineral phase) vs. C (organic phase), as well as the spatial distribution of trace elements such as Na and Mg (Langelier et al., 2017). Using bone samples with known collagen fibril orientation from the femoral cortex, Lee et al. were able to

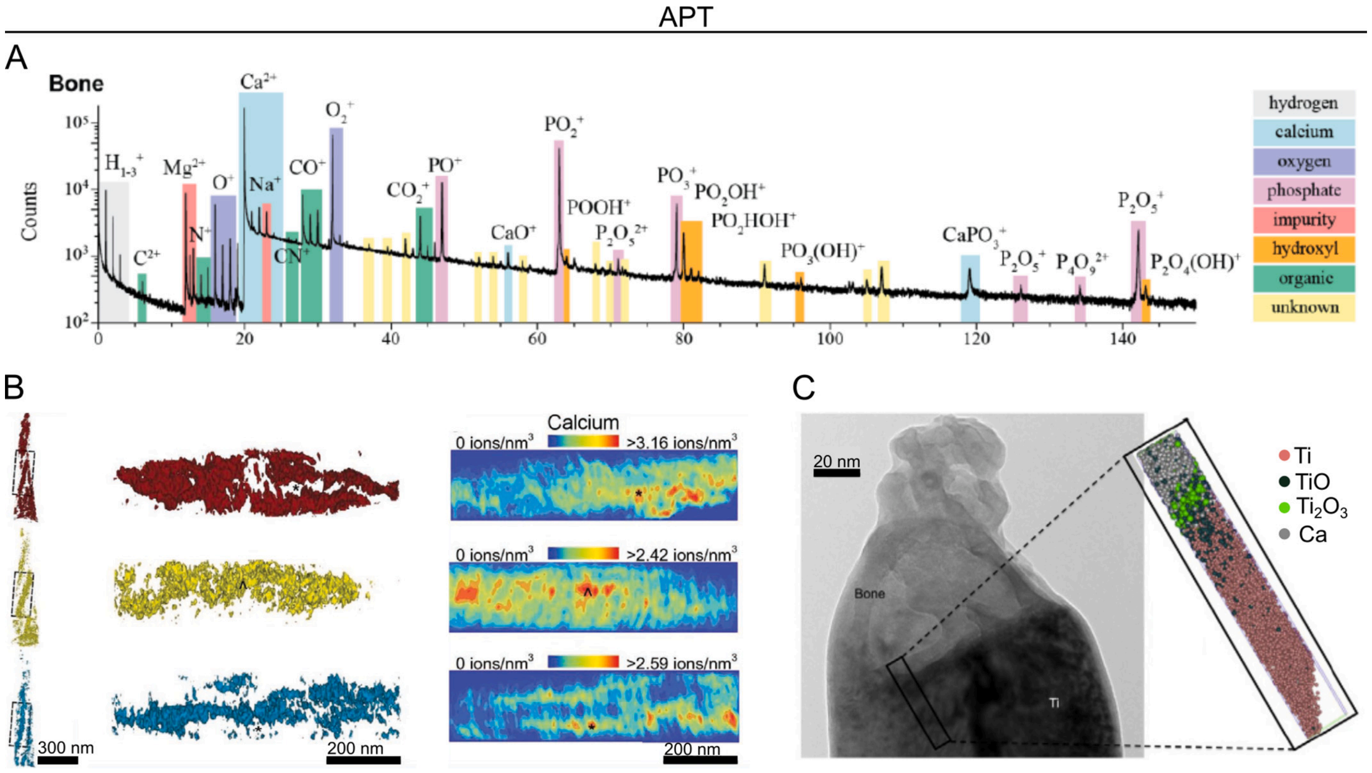

Fig. 6. 4D characterization at the (sub)nanoscale with APT. A) Typical APT spectrum of bone [adapted from Gordon et al. (2012) (see Supporting information) with permission, Copyright 2012, American Chemical Society]. B) Three segmented APT datasets (red, yellow, and cyan) from which individual mineralized collagen fibrils were extracted. Ca atomic density maps (right side of B) evaluated in each of them show both intra- and extra-fibrillar mineralization [adapted from Lee et al. (2021) with permission, Copyright 2021, John Wiley & Sons]. C) BF-TEM image of a bone-titanium implant interface and corresponding APT reconstruction [adapted from Sundell et al. (2017) with permission, Copyright 2016, Elsevier].

precisely locate mineral constituents (Ca and P) in relation to individual collagen fibrils to demonstrate intra- and extra-fibrillar mineralization, also providing evidence of the existence of amorphous calcium phosphate in the gap regions (Lee et al., 2021) (Fig. 6B). APT also proved to be a valid tool to characterize biointerfaces, revealing atomic continuity between bone and osseointegrated implants. Various bone-biomaterial interfaces have been characterized with APT, ranging from titanium with various surface modifications (mesoporous oxide coatings (Karlsson et al., 2014), sand-blasted and acid-etched surfaces (Sundell et al., 2017; Kim et al., 2018), laser-ablated surfaces (X. Wang et al., 2018a)) to bioceramics (Holmes et al., 2023) (Fig. 6C). Interestingly, various studies reported bone mineral-related Ca but scarce organics immediately at the implant surface, suggesting that there is no protein mediation in bone bonding to titanium (Karlsson et al., 2014; Sundell et al., 2017; Kim et al., 2018). APT has also been valuable to resolve the elements present in small amounts otherwise not detectable with other techniques, for example the N-enriched surface layer of a commercial, laser-ablated dental implant (X. Wang et al., 2018a). Notably, this study also correlates APT with on-axis electron tomography and EELS tomography (X. Wang et al., 2018a).

6. Future perspectives

The mechanical function of bone is intimately tied to the structure and composition. Across the macro-, micro-, and nanoscale, structural information obtained using micro−/nano-CT, X-ray scattering, and electron microscopy helps us understand how bone withstands mechanical stress and resists crack propagation. The composition, on the other hand, for example determined using EDX, EELS, vibrational spectroscopy, and mass spectrometry informs us about how the variations in organic and inorganic composition influence mechanical properties such as stiffness, hardness, and interfacial strength. From a materials science perspective, the major focus is on the properties of bone at the extracellular matrix level, which could serve as a potential therapeutic target. It is important to note that both the mineral phase and the organic matrix (collagen, non-collagenous proteins), the degree of mineralization, the presence of water, and the overall architecture influence the mechanical properties of bone. Each of these factors plays a fundamental role in bone material properties and changes in any of these can significantly impact bone health and function.

6.1. Correlative approaches, sample size, and representativity

As a trade-off exists between resolution and the field of view/volume of material that can be analyzed (see Fig. 1), a multiscale approach is best suited to investigate bone material properties (structure and composition) across its hierarchical architecture. Typically, one length scale or a sub-set of length scales is targeted in studies addressing specific research questions. In this scenario, a top-down approach going from larger to smaller length scales is advisable, especially combining different techniques in a correlative manner. This is particularly valuable for making informed decisions on the selection of regions of interest for subsequent higher-resolution analyses. At the same time, there may be concerns about whether the limited volume of material analyzed accurately represents the entire sample. While representativity issues can be mitigated by increasing the number of observations, e.g., by examining multiple samples or obtaining samples from different individuals, the characterization techniques accessing nanoscale information reviewed herein, S/TEM and APT, require labor-intensive and expensive sample preparation usually involving lift-outs in dual-beam FIB-SEM instruments (Jarmar et al., 2008; Huang et al., 2014). This in turn restricts the sample size, and these studies are often qualitative or only semi-quantitative, with limited statistical analyses. Automated tools for S/TEM sample preparation are available and can afford higher throughput without compromising sample quality (Tsurusawa et al., 2021). However, they have not been tested yet on bone, which introduces additional challenges related to electron beam sensitivity and bone-biomaterial interfaces involving materials that experience dissimilar ion milling rates. Data and image analysis can become a cumbersome task, especially for complex features such as collagen-mineral interfaces at the nanoscale, or for large and multidimensional datasets, for instance P/FIB-SEM tomograms. In this regard, (semi) automated tools based on deep learning can become a powerful asset in image processing and analysis, especially for image segmentation to retrieve quantitative information (Reznikov et al., 2020).

6.2. Clinical relevance

Limited sample size combined with potential artifacts arising from sample preservation and preparation, e.g., dehydration and fixation (Shah et al., 2015b), is a particularly relevant consideration when addressing biological and clinical questions. An intact bone-implant interface is an important prerequisite for high resolution examination of the interface (Palmquist et al., 2012a). Unfortunately, where TEM specimens are obtained using FIB instrumentation, distortion and separation at the bone-implant interface make accurate analysis impossible (Palmquist et al., 2009b, 2011). Although most techniques discussed herein are ex situ, it is important to understand how to interpret the findings in relation to the in vivo scenario. For example, qBEI has been validated as a tool to determine bone mineral density distribution (or BMDD) in clinical biopsies (Roschger et al., 1998, 2008), and calcium content (in wt%) thus obtained has been shown to be in good correlation with the mineral-to-matrix ratio determined through Raman spectroscopy (Roschger et al., 2014).

Taking one step forward, bone quality parameters measured under ex situ conditions must be connected to tissue quality in vivo. An emerging application is that of transcutaneous Raman spectroscopy, which has been successfully tested for phalangeal bones in human fingers, where bone quality parameters have been found to correlate with distal radius fracture strength (Massie et al., 2023). While this opens possibilities for longitudinal studies, where bone quality can be directly assessed in living human and animal tissue, the overlying tissue (e.g., skin) tends to obscure the signal from bone and melanin in the skin generates a fluorescence background in the Raman spectrum (Schulmerich et al., 2006). Similarly, in vivo micro-CT has been used for the characterization of bone architecture in living animals, for example to monitor the progression of degenerative conditions such as osteoarthritis (Mohan et al., 2011) and bone regeneration in response to implanted biomaterials (Lienemann et al., 2015). Nevertheless, both techniques hold great potential for clinical translation and application in living individuals.

6.3. Considerations on the hydration state

Although water is an essential component of bone, traditional imaging techniques such as histology and electron microscopy often overlook water due to sample dehydration. It is important to recognize that water significantly impacts the material properties, tissue-level mechanics, and biomechanics of bone (Granke et al., 2015). Moreover, at the nanoscale, water plays a fundamental role in the structuring of bone apatite (Wang et al., 2013). This water-mediated structuring has profound implications for both the mechanical and biological functions of bone. Under experimental conditions, dehydration affects the dimensions of lamellar bone anisotropically, strongly suggesting that examining bone under hydrated conditions can provide a more accurate representation of the natural state (Utku et al., 2008). The use of ionic liquids presents a novel approach for preparing and imaging bone in a hydrated state using SEM (DiCecco et al., 2021). Distinct water compartments, e.g., matrix-bound and unbound water, within bone have been identified using Raman spectroscopy, providing insights into their respective roles in bone structure and function (Unal et al., 2014). Solid-state nuclear magnetic resonance spectroscopy (ssNMR), magnetic resonance imaging (MRI), and photoacoustic imaging also reveal information on bone hydration levels, which could be a potential therapeutic target for enhancing bone strength and resilience, underscoring the importance of considering water in studying bone health and development of interventions aimed at improving bone quality (Surowiec et al., 2022).

6.4. Correlating structure and mechanical properties in mechanical models

Simple mechanical models tend to have significant limitations and often fail to consider the impact of specific structures and building blocks, such as the arrangement of mineral particles into micrometer-sized ellipsoids/tesselles (Binkley et al., 2020; Buss et al., 2020; Micheletti et al., 2022a; Shah et al., 2020). Furthermore, often overlooked is the concept of crossfibrillar tessellation (Buss et al., 2020), that such ellipsoids/tesselles are packed in 3D while retaining organic gaps in between, which make them appear as discrete, quantifiable entities (McKee et al., 2022). This organic-inorganic organization not only plays a central role in the periodicity of the lamellar architecture but is bound to affect the (sub)micro-mechanical behavior of bone. The relationship between the osteocyte LCN architecture and progression of mineralization is well understood, at least in lamellar bone (Ayoubi et al., 2021), but this too, is often ignored by mechanical models. Yet another parameter not taken into consideration is the precise distribution of the mineral within and around the collagen fibrils, where most of the mineral resides extra-fibrillarly (Schwarcz et al., 2017). However, many mechanical models are oversimplified and assume a constant or progressively varying mineral volume fraction (Wang and Ural, 2018), without discriminating between the intra-fibrillar and extra-fibrillar mineral volume fractions and their potential individual mechanical contributions.

6.5. Real-time investigations: in situ and in operando approaches

Ex situ “static” analyses provide useful insights but only offer a snapshot of a specific instance in the sample history, which is highly relevant to a dynamic tissue such as bone. Particularly in the case of bone regeneration, it is challenging to compare bone properties across species and healing time points, and a concept of *fractional age* has been proposed to enable comparisons between species of widely divergent lifespans (Ravaglioli et al., 1996). Real-time investigations by means of in situ and *in operando* approaches can reveal powerful information on how dynamic processes occur as a function of time, and truly represent the final frontier.

For example, liquid and in situ TEM have been used to observe calcium phosphate formation (X. Wang et al., 2018b) and collagen mineralization (DiCecco et al., 2023) and in “real” time, as opposed to cryo-electron tomography (Nudelman et al., 2010). While experimental conditions are still not close to the real environment, these techniques can offer important information on where the mineralization of collagen fibrils begins (inside or outside?), and how different non-collagenous proteins can modulate this process, which can be especially relevant for mineralization in pathological conditions. Continuous monitoring in liquid confirms that calcium phosphate formation from simulated body fluid occurs by particle attachment (X. Wang et al., 2018b). The use of custom thin-film enclosures has also enabled visualization of the mineralization of reconstituted collagen fibrils in a calcium phosphate solution, where mineral particles initially attach to the collagen fibrils and progress to crystalline mineral platelets aligned with the collagen fibrils (DiCecco et al., 2023).

Collagen mineralization has also been investigated with X-ray scattering methods to better understand the mechanical stress evolution (Ping et al., 2022). Real-time tensile testing has shown that the collagen triple helix undergoes conformational changes upon dehydration, causing contraction of the molecule with substantial forces. Tensile stresses thus generated, i.e., during mineralization, are directly responsible for the compressive stresses measured in bone mineral, where higher strains are measured when the mineral content is lower (Bertinetti et al., 2015). In situ SAXS/WAXS experiments reveal that, under tensile loading, the hierarchical design of bone at the nanometer scale leads to a coupled deformation mechanism between collagen fibrils and mineral platelets, resulting in load sharing and damage shielding, thereby preventing the collagen fibrils from exposure to excessive strains (Gupta et al., 2006). Moreover, collagen fibril orientation relative to tensile loading has been shown to influence the strain magnitude, such that higher strains are measured (in both the collagen fibrils and the mineral platelets) when loaded along the fiber direction (Gustafsson et al., 2018).

Finally, mechanical testing using atomic force microscopy (Jimenez-Palomar et al., 2015) and nanoindentation (Tertuliano and Greer, 2016) of FIB-milled micropillars together with direct visualization in the SEM has enabled a better understanding of the variation in mechanical properties such as elastic modulus, strength, and work to fracture in relation to collagen fibril orientation (Jimenez-Palomar et al., 2015). Such experiments also have also highlighted the so-called ‘*smaller-is-stronger*’ size effect, where test samples of 250 nm diameter exhibit over 2-fold higher strength than test samples of 500 nm diameter (Tertuliano and Greer, 2016).

CRediT authorship contribution statement

Chiara Micheletti: Writing – original draft, Visualization, Conceptualization. **Furqan A. Shah:** Writing – original draft, Visualization, Funding acquisition, Conceptualization.

Declaration of competing interest

The authors declare that they have no known competing financial interests or personal relationships that could have appeared to influence the work reported in this paper.

Data availability

Data will be made available on request.

Acknowledgements

Financial support from the Svenska Sällskapet för Medicinsk Forskning (SSMF), the Ingabritt and Arne Lundberg Research Foundation, the Adlerbertska Foundation, the Hjalmar Svensson Foundation, and Kungliga Vetenskaps-och Vitterhets-Samhället i Göteborg is acknowledged.

References

Åkesson, K., Grynpas, M.D., Hancock, R.G.V., Odselius, R., Obrant, K.J., 1994. Energy-dispersive X-ray microanalysis of the bone mineral content in human trabecular bone: a comparison with ICPES and neutron activation analysis. Calcif. Tissue Int. 55, 236–239.

Albrektsson, T., Brånemark, P.I., Hansson, H.A., Lindström, J., 1981. Osseointegrated titanium implants: requirements for ensuring a long-lasting, direct bone-to-implant anchorage in man. Acta Orthop. Scand. 52, 155–170.

Alexander, B., Daulton, T.L., Genin, G.M., Lipner, J., Pasteris, J.D., Wopenka, B., et al., 2012. The nanometre-scale physiology of bone: steric modelling and scanning transmission electron microscopy of collagen–mineral structure. J. R. Soc. Interface. 9, 1774–1786.

Arsenault, A.L., 1989. A comparative electron microscopic study of apatite crystals in collagen fibrils of rat bone, dentin and calcified turkey leg tendons. Bone Miner. 6, 165–177.

Arsenault, A.L., Ottensmeyer, F.P., 1983. Quantitative spatial distributions of calcium, phosphorus, and sulfur in calcifying epiphysis by high resolution electron spectroscopic imaging. Proc. Natl. Acad. Sci. USA 80, 1322–1326.

Ascenzi, A., Bonucci, E., 1968. The compressive properties of single osteons. Anat. Rec. 161, 377–391.

Ayoubi, M., Tol, A.F., Weinkamer, R., Roschger, P., Brugger, P.C., Berzlanovich, A., et al., 2021. 3D interrelationship between osteocyte network and forming mineral during human bone remodeling. Adv. Healthc. Mater. 10, 2100113.

Ayukawa, Y., Takeshita, F., Inoue, T., Yoshinari, M., Shimono, M., Suetsugu, T., et al., 1998. An immunoelectron microscopic localization of noncollagenous bone proteins (osteocalcin and osteopontin) at the bone–titanium interface of rat tibiae. J. Biomed. Mater. Res. 41, 111–119.

Bals, S., Aert, S.V., Tendeloo, G.V., 2013. High resolution electron tomography. Curr. Opin. Solid State Mater. Sci. 17, 107–114.

Bertinetti, L., Masic, A., Schuetz, R., Barbetta, A., Seidt, B., Wagermaier, W., et al., 2015. Osmotically driven tensile stress in collagen-based mineralized tissues. J. Mech. Behav. Biomed. Mater. 52, 14–21.

Binkley, D.M., Grandfield, K., 2017. Progress and trends in characterization of biomineralized tissues and biomaterials interfaces. ACS Biomater Sci. Eng. 4, 3678–3690.

Binkley, D.M., Deering, J., Yuan, H., Gourrier, A., Grandfield, K., 2020. Ellipsoidal mesoscale mineralization pattern in human cortical bone revealed in 3D by plasma focused ion beam serial sectioning. J. Struct. Biol. 212, 107615.

Blank, R.D., Baldini, T.H., Kaufman, M., Bailey, S., Gupta, R., Yershov, Y., et al., 2003. Spectroscopically determined collagen Pyr/deH-DHLNL cross-link ratio and crystallinity indices differ markedly in recombinant congenic mice with divergent calculated bone tissue strength. Connect. Tissue Res. 44, 134–142.

Bocciarelli, D.S., 1970. Morphology of crystallites in bone. Calcif. Tissue Res. 5, 261–269.

Bohner, M., Baroud, G., Bernstein, A., Döbelin, N., Galea, L., Hesse, B., et al., 2017. Characterization and distribution of mechanically competent mineralized tissue in micropores of β-tricalcium phosphate bone substitutes. Mater. Today 20, 106–115.

Bonewald, L.F., 2011. The amazing osteocyte. J. Bone Miner. Res. 26, 229–238.

Boskey, A., Mendelsohn, R., 2005a. Infrared analysis of bone in health and disease. J. Biomed. Opt. 10, 031102.

Boskey, A.L., Mendelsohn, R., 2005b. Infrared spectroscopic characterization of mineralized tissues. Vib. Spectrosc. 38, 107–114.

Boskey, A.L., Reddi, A.H., 1983. Changes in lipids during matrix: induced endochondral bone formation. Calcif. Tissue Int. 35, 549–554.

Boskey, A.L., DiCarlo, E., Paschalis, E., West, P., Mendelsohn, R., 2005. Comparison of mineral quality and quantity in iliac crest biopsies from high- and low-turnover osteoporosis: an FT-IR microspectroscopic investigation. Osteoporos. Int. 16, 2031–2038.

Bousson, V., Peyrin, F., Bergot, C., Hausard, M., Sautet, A., Laredo, J., 2004. Cortical bone in the human femoral neck: three-dimensional appearance and porosity using synchrotron radiation. J. Bone Miner. Res. 19, 794–801.

Bouxsein, M.L., Boyd, S.K., Christiansen, B.A., Guldberg, R.E., Jepsen, K.J., Müller, R., 2010. Guidelines for assessment of bone microstructure in rodents using micro-computed tomography. J. Bone Miner. Res. 25, 1468–1486.

Boyde, A., 2019. Scanning electron microscopy of bone. In: Idris, A.I. (Ed.), Bone Research Protocols, Methods in Molecular Biology, pp. 571–616.

Boyde, A., Riggs, C.M., 1990. The quantitative study of the orientation of collagen in compact bone slices. Bone 11, 35–39.

Boyde, A., Howell, P., Bromage, T., Elliott, J., Riggs, C., Bell, L., et al., 1992. Application of mineral quantitation of bone by histogram analysis of backscattered electron images. In: Slavkin, H., Price, P. (Eds.), Excerpta Medica Int Congr Ser ICS 1002. Elsevier, Amsterdam, pp. 47–60.

Brånemark, P.I., Hansson, B.O., Adell, R., Breine, U., Lindström, J., Hallén, O., et al., 1977. Osseointegrated implants in the treatment of the edentulous jaw. Experience from a 10-year period. Scand. J. Plast. Reconstr. Surg. Suppl. 16, 1–132.

Bromage, T.G., Goldman, H.M., McFarlin, S.C., Warshaw, J., Boyde, A., Riggs, C.M., 2003. Circularly polarized light standards for investigations of collagen fiber orientation in bone. Anat Rec Part B: N Anat. 274B, 157–168.

Budd, T., Nagahara, K., Bielat, K., Meenaghan, M., Schaaf, N., 1992. Visualization and initial characterization of the titanium boundary of the bone-implant interface of osseointegrated implants. Int. J. Oral Maxillofac. Implants 7, 151–160.

Burnett, T.L., Kelley, R., Winiarski, B., Contreras, L., Daly, M., Gholinia, A., et al., 2016. Large volume serial section tomography by Xe Plasma FIB dual beam microscopy. Ultramicroscopy 161, 119–129.

Buss, D.J., Reznikov, N., McKee, M.D., 2020. Crossfibrillar mineral tessellation in normal and Hyp mouse bone as revealed by 3D FIB-SEM microscopy. J. Struct. Biol. 212, 107603.

Buss, D.J., Kröger, R., McKee, M.D., Reznikov, N., 2022. Hierarchical organization of bone in three dimensions: a twist of twists. J Struct Biol X. 6, 100057.

Cantoni, M., Holzer, L., 2014. Advances in 3D focused ion beam tomography. MRS Bull. 39, 354–360.

Carden, A., Rajachar, R.M., Morris, M.D., Kohn, D.H., 2003. Ultrastructural changes accompanying the mechanical deformation of bone tissue: a Raman imaging study. Calcif. Tissue Int. 72, 166–175.

Carter, C.B., Williams, D.B., 2016. Imaging in STEM. In: Carter, C.B., Williams, D.B. (Eds.), Transmission Electron Microscopy Diffraction, Imaging and Spectrometry. Springer, New York, NY.

Collins, S.M., Midgley, P.A., 2017. Progress and opportunities in EELS and EDS tomography. Ultramicroscopy 180, 133–141.

Cooper, D.M.L., Thomas, C.D.L., Clement, J.G., Hallgrímsson, B., 2006. Three-dimensional microcomputed tomography imaging of basic multicellular unit-related resorption spaces in human cortical bone. Anat. Rec. Part A: Discov. Mol. Cell. Evol. Biol. 288A, 806–816.

Cressey, B.A., Cressey, G., 2003. A model for the composite nanostructure of bone suggested by high-resolution transmission electron microscopy. Mineral. Mag. 67, 1171–1182.

Deering, J., Chen, J., Mahmoud, D., Tang, T., Lin, Y., Fang, Q., et al., 2023. Characterizing mineral ellipsoids in new bone formation at the interface of Ti6Al4V porous implants. Adv. Mater. Interfaces 10, 2300333.

Deshpande, A.S., Beniash, E., 2008. Bioinspired synthesis of mineralized collagen fibrils. Cryst. Growth Des. 8, 3084–3090.

DiCecco, L.A., D'Elia, A., Quenneville, C., Soleymani, L., Grandfield, K., 2021. Ionic liquid treatment for efficient sample preparation of hydrated bone for scanning electron microscopy. Micron 153, 103192.

DiCecco, L.A., Gao, R., Gray, J.L., Kelly, D.F., Sone, E.D., Grandfield, K., 2023. Liquid transmission electron microscopy for probing collagen biomineralization. Nano Lett. 21, 9760–9768.

Donnelly, E., Chen, D.X., Boskey, A.L., Baker, S.P., van der Meulen, M.C.H., 2010. Contribution of mineral to bone structural behavior and tissue mechanical properties. Calcif. Tissue Int. 87, 450–460.

Egerton, R.F., 2011. Electron Energy-loss Spectroscopy in the Electron Microscope. Springer, New York, NY.

Ercius, P., Alaidi, O., Rames, M.J., Ren, G., 2015. Electron tomography: a three-dimensional analytic tool for hard and soft materials research. Adv. Mater. 27, 5638–5663.

Faingold, A., Cohen, S.R., Reznikov, N., Wagner, H.D., 2013. Osteonal lamellae elementary units: lamellar microstructure, curvature and mechanical properties. Acta Biomater. 9, 5956–5962.

Fearn, S., 2015. An Introduction to Time-of-flight Secondary Ion Mass Spectrometry (ToF-SIMS) and Its Application to Materials Science. Morgan & Claypool Publishers, San Rafael, CA.

Fratzl, P., Weinkamer, R., 2007. Nature's hierarchical materials. Prog. Mater. Sci. 52, 1263–1334.

Fratzl, P., Schreiber, S., Klaushofer, K., 1996. Bone mineralization as studied by small-angle X-ray scattering. Connect. Tissue Res. 34, 247–254.

Fratzl, P., Gupta, H.S., Paschalis, E.P., Roschger, P., 2004. Structure and mechanical quality of the collagen–mineral nano-composite in bone. J. Mater. Chem. 14, 2115–2123.

Frushour, B.G., Koenig, J.L., 1975. Raman scattering of collagen, gelatin, and elastin. Biopolymers 14, 379–391.

Gadaleta, S.J., Paschalis, E.P., Betts, F., Mendelsohn, R., Boskey, A.L., 1996. Fourier transform infrared spectroscopy of the solution-mediated conversion of amorphous calcium phosphate to hydroxyapatite: new correlations between X-ray diffraction and infrared data. Calcif. Tissue Int. 58, 9–16.

Gamsjaeger, S., Masic, A., Roschger, P., Kazanci, M., Dunlop, J.W.C., Klaushofer, K., et al., 2010. Cortical bone composition and orientation as a function of animal and tissue age in mice by Raman spectroscopy. Bone 47, 392–399.

Gamsjaeger, S., Buchinger, B., Zwettler, E., Recker, R., Black, D., Gasser, J.A., et al., 2011. Bone material properties in actively bone-forming trabeculae in postmenopausal women with osteoporosis after three years of treatment with once-yearly Zoledronic acid. J. Bone Miner. Res. 26, 12–18.

Gamsjaeger, S., Brozek, W., Recker, R., Klaushofer, K., Paschalis, E.P., 2014a. Transmenopausal changes in trabecular bone quality. J. Bone Miner. Res. 29, 608–617.

Gamsjaeger, S., Srivastava, A.K., Wergedal, J.E., Zwerina, J., Klaushofer, K., Paschalis, E. P., et al., 2014b. Altered bone material properties in HLA-B27 rats include reduced mineral to matrix ratio and altered collagen cross-links. J. Bone Miner. Res. 29, 2382–2391.

Gamsjaeger, S., Robins, S.P., Tatakis, D.N., Klaushofer, K., Paschalis, E.P., 2017. Identification of pyridinoline trivalent collagen cross-links by Raman microspectroscopy. Calcif. Tissue Int. 100, 565–574.

Gault, B., Chiaramonti, A., Cojocaru-Mirédin, O., Stender, P., Dubosq, R., Freysoldt, C., et al., 2021. Atom probe tomography. Nat. Rev. Methods Prim. 1, 51.

Genthial, R., Beaurepaire, E., Schanne-Klein, M.C., Peyrin, F., Farlay, D., Olivier, C., et al., 2017. Label-free imaging of bone multiscale porosity and interfaces using third-harmonic generation microscopy. Sci. Rep. 7, 3419.

Georgiadis, M., Müller, R., Schneider, P., 2016. Techniques to assess bone ultrastructure organization: orientation and arrangement of mineralized collagen fibrils. J. R. Soc. Interface. 13, 20160088.

Giannuzzi, L.A., Giannuzzi, N.J., Capuano, M.J., 2005. FIB, SEM, and TEM of bone/dental implant interfaces. Microsc. Microanal. 11, 998–999.

Goldberg, M., Boskey, A.L., 1996. Lipids and biomineralizations. Prog. Histochem. Cytochem. 31, III–187.

Goldman, H.M., Kindsvater, J., Bromage, T.G., 1999. Correlative light and backscattered electron microscopy of bone—part I: specimen preparation methods. Scanning 21, 40–43.

Goldstein, J.I., Newbury, D.E., Michael, J.R., Ritchie, N.W.M., Scott, J.H.J., Joy, D.C., 2018. Scanning electron Microscopy and X-ray Microanalysis. Springer, New York, NY.

Gordon, L.M., Tran, L., Joester, D., 2012. Atom probe tomography of apatites and bone-type mineralized tissues. ACS Nano 6, 10667–10675.

Gourion-Arsiquaud, S., Faibish, D., Myers, E., Spevak, L., Compston, J., Hodsman, A., et al., 2009. Use of FTIR spectroscopic imaging to identify parameters associated with fragility fracture. J. Bone Miner. Res. 24, 1565–1571.

Grandfield, K., 2015. Bone, implants, and their interfaces. Phys. Today 68, 40–45.

Grandfield, K., Engqvist, H., 2012. Focused ion beam in the study of biomaterials and biological matter. Adv. Mater. Sci. Eng. 2012, 1–6.

Grandfield, K., McNally, E.A., Palmquist, A., Botton, G.A., Thomsen, P., Engqvist, H., 2010. Visualizing biointerfaces in three dimensions: electron tomography of the bone-hydroxyapatite interface. J. R. Soc. Interface 7, 1497–1501.

Grandfield, K., Palmquist, A., Engqvist, H., 2012. High-resolution three-dimensional probes of biomaterials and their interfaces. Philos. Trans. R. Soc. A Math. Phys. Eng. Sci. 370, 1337–1351.

Grandfield, K., Gustafsson, S., Palmquist, A., 2013a. Where bone meets implant: the characterization of nano-osseointegration. Nanoscale 5, 4302–4308.

Grandfield, K., Palmquist, A., Engqvist, H., 2013b. Three-dimensional structure of laser-modified Ti6Al4V and bone interface revealed with STEM tomography. Ultramicroscopy 127, 48–52.

Grandfield, K., Vuong, V., Schwarcz, H.P., 2018. Ultrastructure of bone: hierarchical features from nanometer to micrometer scale revealed in focused ion beam sections in the TEM. Calcif. Tissue Int. 103, 606–616.

Grandfield, K., Micheletti, C., Deering, J., Arcuri, G., Tang, T., Langelier, B., 2022. Atom probe tomography for biomaterials and biomineralization. Acta Biomater. 148, 44–60.

Granke, M., Does, M.D., Nyman, J.S., 2015. The role of water compartments in the material properties of cortical bone. Calcif. Tissue Int. 97, 292–307.

Grünewald, T.A., Johannes, A., Wittig, N.K., Palle, J., Rack, A., Burghammer, M., et al., 2023. Bone mineral properties and 3D orientation of human lamellar bone around cement lines and the Haversian system. IUCrJ 10, 189–198.

Guagliardi, A., Giannini, C., Cedola, A., Mastrogiacomo, M., Ladisa, M., Cancedda, R., 2009. Toward the X-ray microdiffraction imaging of bone and tissue-engineered bone. Tissue Eng. Part B Rev. 15, 423–442.

Gupta, H.S., Seto, J., Wagermaier, W., Zaslansky, P., Boesecke, P., Fratzl, P., 2006. Cooperative deformation of mineral and collagen in bone at the nanoscale. Proc. Natl. Acad. Sci. USA 103, 17741–17746.

Gustafsson, A., Mathavan, N., Turunen, M.J., Engqvist, J., Khayyeri, H., Hall, S.A., et al., 2018. Linking multiscale deformation to microstructure in cortical bone using in situ loading, digital image correlation and synchrotron X-ray scattering. Acta Biomater. 69, 323–331.

Henss, A., Rohnke, M., Khassawna, T.E., Govindarajan, P., Schlewitz, G., Heiss, C., et al., 2013. Applicability of ToF-SIMS for monitoring compositional changes in bone in a long-term animal model. J. R. Soc. Interface 10, 20130332.

Hodge, A.J., Petruska, J.A., 1963. Recent studies with the electron microscope on ordered aggregates of the tropocollagen macromolecule. In: Ramachandran, G.N. (Ed.), Aspects of Protein Structure. Academic Press, New York, NY, pp. 289–300.

Holmes, N.P., Roohani, I., Entezari, A., Guagliardo, P., Mirkhalaf, M., Lu, Z., et al., 2023. Discovering an unknown territory using atom probe tomography: elemental exchange at the bioceramic scaffold/bone tissue interface. Acta Biomater. 162, 199–210.

Hoshi, K., Ejiri, S., Ozawa, H., 2001. Localizational alterations of calcium, phosphorus, and calcification-related organics such as proteoglycans and alkaline phosphatase during bone calcification. J. Bone Miner. Res. 16, 289–298.

Huang, R.Y., Miller, L.M., Carlson, C.S., Chance, M.R., 2003. In situ chemistry of osteoporosis revealed by synchrotron infrared microspectroscopy. Bone 33, 514–521.

Huang, J., Wang, X., Grandfield, K., 2014. FIB preparation of bone-implant interfaces for correlative on-axis rotation electron tomography and atom probe tomography. Microsc. Microanal. 20, 352–353.

Jantou, V., Turmaine, M., West, G.D., Horton, M.A., McComb, D.W., 2009. Focused ion beam milling and ultramicrotomy of mineralised ivory dentine for analytical transmission electron microscopy. Micron 40, 495–501.

Jantou-Morris, V., Horton, M.A., McComb, D.W., 2010. The nano-morphological relationships between apatite crystals and collagen fibrils in ivory dentine. Biomaterials 31, 5275–5286.

Jarmar, T., Palmquist, A., Brånemark, R., Hermansson, L., Engqvist, H., Thomsen, P., 2008. Technique for preparation and characterization in cross-section of oral titanium implant surfaces using focused ion beam and transmission electron microscopy. J. Biomed. Mater. Res. A 87A, 1003–1009.

Jimenez-Palomar, I., Shipov, A., Shahar, R., Barber, A.H., 2015. Structural orientation dependent sub-lamellar bone mechanics. J. Mech. Behav. Biomed. Mater. 52, 63–71.

Karlsson, J., Sundell, G., Thuvander, M., Andersson, M., 2014. Atomically resolved tissue integration. Nano Lett. 14, 4220–4223.

Kawase, N., Kato, M., Nishioka, H., Jinnai, H., 2007. Transmission electron microtomography without the "missing wedge" for quantitative structural analysis. Ultramicroscopy 107, 8–15.

Kazanci, M., Roschger, P., Paschalis, E.P., Klaushofer, K., Fratzl, P., 2006a. Bone osteonal tissues by Raman spectral mapping: orientation–composition. J. Struct. Biol. 156, 489–496.

Kazanci, M., Fratzl, P., Klaushofer, K., Paschalis, E.P., 2006b. Complementary information on in vitro conversion of amorphous (precursor) calcium phosphate to hydroxyapatite from Raman microspectroscopy and wide-angle X-ray scattering. Calcif. Tissue Int. 79, 354–359.

Kim, J.S., Kang, S.M., Seo, K.W., Nahm, K.Y., Chung, K.R., Kim, S.H., et al., 2015. Nanoscale bonding between human bone and titanium surfaces: osseohybridization. Biomed. Res. Int. 2015, 960410.

Kim, J.S., Ahn, J.P., Kim, Y.H., Seo, K.W., Zadeh, H., Kim, S.H., 2018. Atomic layout of an orthodontic titanium mini-implant in human tissue: Angle Orthod. 89, 292–298.

Knott, L., Bailey, A.J., 1998. Collagen cross-links in mineralizing tissues: a review of their chemistry, function, and clinical relevance. Bone 22, 181–187.

Landis, W.J., Song, M.J., 1991. Early mineral deposition in calcifying tendon characterized by high voltage electron microscopy and three-dimensional graphic imaging. J. Struct. Biol. 107, 116–127.

Landis, W.J., Song, M.J., Leith, A., McEwen, L., McEwen, B.F., 1993. Mineral and organic matrix interaction in normally calcifying tendon visualized in 3D by HV EM tomography and graphic image reconstruction. J. Struct. Biol. 110, 39–54.

Landis, W.J., Hodgens, K.J., Song, M.J., Arena, J., Kiyonaga, S., Marko, M., et al., 1996a. Mineralization of collagen may occur on fibril surfaces: evidence from conventional and high-voltage electron microscopy and three-dimensional imaging. J. Struct. Biol. 117, 24–35.

Landis, W.J., Hodgens, K.J., Arena, J., Song, M.J., McEwen, B.F., 1996b. Structural relations between collagen and mineral in bone as determined by high voltage electron microscopic tomography. Microsc. Res. Tech. 33, 192–202.

Langelier, B., Wang, X., Grandfield, K., 2017. Atomic scale chemical tomography of human bone. Sci. Rep. 7, 39958.

Lee, B.E.J., Luo, L., Grandfield, K., Andrei, C.M., Schwarcz, H.P., 2019. Identification of collagen fibrils in cross sections of bone by electron energy loss spectroscopy (EELS). Micron 124, 102706.

Lee, B.E.J., Langelier, B., Grandfield, K., 2021. Visualization of collagen–mineral arrangement using atom probe tomography. Adv. Biology. 5, 2100657.

Leeuwenhoek, A.V., 1721. II. Observations upon the bones and the periosteum, in a letter to the Royal Society, from Mr. Leeuwenhoek. F. R. S. Philos Trans R Soc Lond. 31, 91–97.

Lienemann, P.S., Metzger, S., Kiveliö, A.S., Blanc, A., Papageorgiou, P., Astolfo, A., et al., 2015. Longitudinal in vivo evaluation of bone regeneration by combined measurement of multi-pinhole SPECT and micro-CT for tissue engineering. Sci. Rep. 5, 10238.

Loundagin, L., Cooper, D., 2022. Towards novel measurements of remodeling activity in cortical bone: implications for osteoporosis and related pharmaceutical treatments. Eur. Cells Mater. 43, 202–227.

Malmberg, P., Lopes, V.R., Billström, G.H., Gallinetti, S., Illies, C., Linder, L.K.B., et al., 2021. Targeted ToF-SIMS analysis of macrophage content from a human cranial triphasic calcium phosphate implant. ACS Appl. Bio Mater. 4, 6791–6798.

Martin, R.B., Ishida, J., 1989. The relative effects of collagen fiber orientation, porosity, density, and mineralization on bone strength. J. Biomech. 22, 419–426.

Massie, C., Knapp, E., Awad, H.A., Berger, A.J., 2023. Detection of osteoporotic-related bone changes and prediction of distal radius strength using Raman spectra from excised human cadaver finger bones. J. Biomech. 161, 111852.

McElderry, J.P., Zhao, G., Khmaladze, A., Wilson, C.G., Franceschi, R.T., Morris, M.D., 2013. Tracking circadian rhythms of bone mineral deposition in murine calvarial organ cultures. J. Bone Miner. Res. 28, 1846–1854.

McKee, M.D., Farach-Carson, M.C., Butler, W.T., Hauschka, P.V., Nanci, A., 1993. Ultrastructural immunolocalization of noncollagenous (osteopontin and osteocalcin) and plasma (albumin and α2HS-glycoprotein) proteins in rat bone. J. Bone Miner. Res. 8, 485–496.

McKee, M.D., Buss, D.J., Reznikov, N., 2022. Mineral tessellation in bone and the stenciling principle for extracellular matrix mineralization. J. Struct. Biol. 214, 107823.

McNally, E.A., Schwarcz, H.P., Botton, G.A., Arsenault, A.L., 2012. A model for the ultrastructure of bone based on electron microscopy of ion-milled sections. PLoS One 7, e29258.

McNally, E., Nan, F., Botton, G.A., Schwarcz, H.P., 2013. Scanning transmission electron microscopic tomography of cortical bone using Z-contrast imaging. Micron 49, 46–53.

McNerny, E.M., Gong, B., Morris, M.D., Kohn, D.H., 2015. Bone fracture toughness and strength correlate with collagen cross-link maturity in a dose-controlled lathyrism mouse model. J. Bone Miner. Res. 30, 455–464.

Micheletti, C., 2023. Multimodal and Multiscale Characterization of Bone and Bone Interfaces in Health and Disease (PhD Thesis). University of Gothenburg.

Micheletti, C., Gomes-Ferreira, P.H.S., Casagrande, T., Lisboa-Filho, P.N., Okamoto, R., Grandfield, K., 2021. From tissue retrieval to electron tomography: nanoscale characterization of the interface between bone and bioactive glass. J. R. Soc. Interface. 18, 20210181.

Micheletti, C., Hurley, A., Gourrier, A., Palmquist, A., Tang, T., Shah, F.A., et al., 2022a. Bone mineral organization at the mesoscale: a review of mineral ellipsoids in bone and at bone interfaces. Acta Biomater. 142, 1–13.

Micheletti, C., DiCecco, L., Wexell, C.L., Binkley, D.M., Palmquist, A., Grandfield, K., et al., 2022b. Multimodal and multiscale characterization of the bone-bacteria interface in a case of medication-related osteonecrosis of the jaw. JBMR Plus 6, e10693.

Micheletti, C., Shah, F.A., Palmquist, A., Grandfield, K., 2023. Ultrastructure and nanoporosity of human bone shown with correlative on-axis electron and spectroscopic tomographies. ACS Nano 17, 24710–24724.

Midgley, P.A., Weyland, M., 2003. 3D electron microscopy in the physical sciences: the development of Z-contrast and EFTEM tomography. Ultramicroscopy 96, 413–431.

Milovanovic, P., Zimmermann, E.A., Vom Scheidt, A., Hoffmann, B., Sarau, G., Yorgan, T., Schweizer, M., Amling, M., Christiansen, S., Busse, B., 2017. The formation of calcified nanospherites during micropetrosis represents a unique mineralization mechanism in aged human bone. Small 13, 1602215.

Mitchell, J., van Heteren, A.H., 2016. A literature review of the spatial organization of lamellar bone. Cr Palevol. 15, 23–31.

Mohan, G., Perilli, E., Kuliwaba, J.S., Humphries, J.M., Parkinson, I.H., Fazzalari, N.L., 2011. Application of in vivo micro-computed tomography in the temporal characterisation of subchondral bone architecture in a rat model of low-dose monosodium iodoacetate-induced osteoarthritis. Arthritis Res. Ther. 13, R210.

Morris, M.D., Mandair, G.S., 2011. Raman assessment of bone quality. Clin. Orthop. Relat. Res. 469, 2160–2169.

Müller, R., 2009. Hierarchical microimaging of bone structure and function. Nat. Rev. Rheumatol. 5, 373–381.

Nudelman, F., Pieterse, K., George, A., Bomans, P.H.H., Friedrich, H., Brylka, L.J., et al., 2010. The role of collagen in bone apatite formation in the presence of hydroxyapatite nucleation inhibitors. Nat. Mater. 9, 1004.

Orgel, J.P.R.O., Miller, A., Irving, T.C., Fischetti, R.F., Hammersley, A.P., Wess, T.J., 2001. The in situ supermolecular structure of type I collagen. Structure 9, 1061–1069.

Oxlund, H., Barckman, M., Ørtoft, G., Andreassen, T.T., 1995. Reduced concentrations of collagen cross-links are associated with reduced strength of bone. Bone 17, S365–S371.

Pacureanu, A., Langer, M., Boller, E., Tafforeau, P., Peyrin, F., 2012. Nanoscale imaging of the bone cell network with synchrotron X-ray tomography: optimization of acquisition setup. Med. Phys. 39, 2229–2238.

Palmquist, A., 2018. A multiscale analytical approach to evaluate osseointegration. J. Mater. Sci. Mater. Med. 29, 60.

Palmquist, A., Jarmar, T., Emanuelsson, L., Brånemark, R., Engqvist, H., Thomsen, P., 2009a. Forearm bone-anchored amputation prosthesis: a case study on the osseointegration. Acta Orthop. 79, 78–85.

Palmquist, A., Lindberg, F., Emanuelsson, L., Brånemark, R., Engqvist, H., Thomsen, P., 2009b. Morphological studies on machined implants of commercially pure titanium and titanium alloy (Ti6Al4V) in the rabbit. J. Biomed. Mater. Res. B Appl. Biomater. 91, 309–319.

Palmquist, A., Lindberg, F., Emanuelsson, L., Brånemark, R., Engqvist, H., Thomsen, P., 2010. Biomechanical, histological, and ultrastructural analyses of laser micro- and nano-structured titanium alloy implants: a study in rabbit. J. Biomed. Mater. Res. A 92A, 1476–1486.

Palmquist, A., Emanuelsson, L., Brånemark, R., Thomsen, P., 2011. Biomechanical, histological and ultrastructural analyses of laser micro- and nano-structured titanium implant after 6 months in rabbit. J. Biomed. Mater. Res. B Appl. Biomater. 97, 289–298.

Palmquist, A., Grandfield, K., Norlindh, B., Mattsson, T., Brånemark, R., Thomsen, P., 2012a. Bone-titanium oxide interface in humans revealed by transmission electron microscopy and electron tomography. J. R. Soc. Interface 9, 396–400.

Palmquist, A., Emanuelsson, L., Sjövall, P., 2012b. Chemical and structural analysis of the bone-implant interface by TOF-SIMS, SEM, FIB and TEM: experimental study in animal. Appl. Surf. Sci. 258, 6485–6494.

Palmquist, A., Shah, F.A., Emanuelsson, L., Omar, O., Suska, F., 2017. A technique for evaluating bone ingrowth into 3D printed, porous Ti6Al4V implants accurately using X-ray micro-computed tomography and histomorphometry. Micron 94, 1–8.

Paris, O., 2008. From diffraction to imaging: new avenues in studying hierarchical biological tissues with X-ray microbeams (review). Biointerphases 3, FB16–26.

Paschalis, E.P., DiCarlo, E., Betts, F., Sherman, P., Mendelsohn, R., Boskey, A.L., 1996. FTIR microspectroscopic analysis of human osteonal bone. Calcif. Tissue Int. 59, 480–487.

Paschalis, E.P., Betts, F., DiCarlo, E., Mendelsohn, R., Boskey, A.L., 1997. FTIR microspectroscopic analysis of human iliac crest biopsies from untreated osteoporotic bone. Calcif. Tissue Int. 61, 487–492.

Paschalis, E.P., Verdelis, K., Doty, S.B., Boskey, A.L., Mendelsohn, R., Yamauchi, M., 2001. Spectroscopic characterization of collagen cross-links in bone. J. Bone Miner. Res. 16, 1821–1828.

Paschalis, E.P., Shane, E., Lyritis, G., Skarantavos, G., Mendelsohn, R., Boskey, A.L., 2004. Bone fragility and collagen cross-links. J. Bone Miner. Res. 19, 2000–2004.

Paschalis, E.P., Glass, E.V., Donley, D.W., Eriksen, E.F., 2005. Bone mineral and collagen quality in iliac crest biopsies of patients given teriparatide: new results from the fracture prevention trial. J. Clin. Endocrinol. Metab. 90, 4644–4649.

Paschalis, E.P., Tatakis, D.N., Robins, S., Fratzl, P., Manjubala, I., Zoehrer, R., et al., 2011. Lathyrism-induced alterations in collagen cross-links influence the mechanical properties of bone material without affecting the mineral. Bone 49, 1232–1241.

Pasteris, J.D., Wopenka, B., Freeman, J.J., Rogers, K., Valsami-Jones, E., van der Houwen, J.A., Silva, M.J., 2004. Lack of OH in nanocrystalline apatite as a function of degree of atomic order: implications for bone and biomaterials. Biomaterials 25, 229–238.

Penel, G., Delfosse, C., Descamps, M., Leroy, G., 2005. Composition of bone and apatitic biomaterials as revealed by intravital Raman microspectroscopy. Bone 36, 893–901.

Pennycook, S.J., 1989. Z-contrast STEM for materials science. Ultramicroscopy 30, 58–69.

Peyrin, F., Dong, P., Pacureanu, A., Langer, M., 2014. Micro- and nano-CT for the study of bone ultrastructure. Curr. Osteoporos. Rep. 12, 465–474.

Pidaparti, R.M.V., Chandran, A., Takano, Y., Turner, C.H., 1996. Bone mineral lies mainly outside collagen fibrils: predictions of a composite model for osteonal bone. J. Biomech. 29, 909–916.

Ping, H., Wagermaier, W., Horbelt, N., Scoppola, E., Li, C., Werner, P., et al., 2022. Mineralization generates megapascal contractile stresses in collagen fibrils. Science 376, 188–192.

Price, P.A., Toroian, D., Lim, J.E., 2009. Mineralization by inhibitor exclusion: the calcification of collagen with fetuin. J. Biol. Chem. 284, 17092–17101.

Raguin, E., Rechav, K., Shahar, R., Weiner, S., 2021. Focused ion beam-SEM 3D analysis of mineralized osteonal bone: lamellae and cement sheath structures. Acta Biomater. 121, 497–513.

Rahmati, M., Stötzel, S., Khassawna, T.E., Mao, C., Ali, A., Vaughan, J.C., et al., 2022. Intrinsically disordered peptides enhance regenerative capacities of bone composite xenografts. Mater. Today 52, 63–79.

Ramasamy, R., Vannucci, S.J., Yan, S.S.D., Herold, K., Yan, S.F., Schmidt, A.M., 2005. Advanced glycation end products and RAGE: a common thread in aging, diabetes, neurodegeneration, and inflammation. Glycobiology 15, 16R–28R.

Ravaglioli, A., Krajewski, A., Celotti, G.C., Piancastelli, A., Bacchini, B., Montanari, L., et al., 1996. Mineral evolution of bone. Biomaterials 17, 617–622.

Reiner, E., Weston, F., Pleshko, N., Querido, W., 2023. Application of optical photothermal infrared (O-PTIR) spectroscopy for assessment of bone composition at the submicron scale. Appl. Spectrosc. 77, 1311–1324.

Reznikov, N., Almany-Magal, R., Shahar, R., Weiner, S., 2013. Three-dimensional imaging of collagen fibril organization in rat circumferential lamellar bone using a dual beam electron microscope reveals ordered and disordered sub-lamellar structures. Bone 52, 676–683.

Reznikov, N., Shahar, R., Weiner, S., 2014a. Bone hierarchical structure in three dimensions. Acta Biomater. 10, 3815–3826.

Reznikov, N., Shahar, R., Weiner, S., 2014b. Three-dimensional structure of human lamellar bone: the presence of two different materials and new insights into the hierarchical organization. Bone 59, 93–104.

Reznikov, N., Bilton, M., Lari, L., Stevens, M.M., Kroger, R., 2018. Fractal-like hierarchical organization of bone begins at the nanoscale. Science 2189, eaao2189.

Reznikov, N., Buss, D.J., Provencher, B., McKee, M.D., Piché, N., 2020. Deep learning for 3D imaging and image analysis in biomineralization research. J. Struct. Biol. 212, 107598.

Ritchie, R.O., Buehler, M.J., Hansma, P., 2009. Plasticity and toughness in bone. Phys. Today 62, 41–47.

Robinson, R.A., 1952. An electron-microscopic study of the crystalline inorganic component of bone and its relationship to the organic matrix. J. Bone Joint Surg. Am. 34-A, 389–434.

Roschger, P., Fratzl, P., Eschberger, J., Klaushofer, K., 1998. Validation of quantitative backscattered electron imaging for the measurement of mineral density distribution in human bone biopsies. Bone 23, 319–326.

Roschger, P., Paschalis, E.P., Fratzl, P., Klaushofer, K., 2008. Bone mineralization density distribution in health and disease. Bone 42, 456–466.

Roschger, A., Gamsjaeger, S., Hofstetter, B., Masic, A., Blouin, S., Messmer, P., et al., 2014. Relationship between the v2PO4/amide III ratio assessed by Raman spectroscopy and the calcium content measured by quantitative backscattered electron microscopy in healthy human osteonal bone. J. Biomed. Opt. 19, 065002.

Sartori, J., Köhring, S., Witte, H., Fischer, M.S., Löffler, M., 2018. Three-dimensional imaging of the fibrous microstructure of Achilles tendon entheses in Mus musculus. J. Anat. 233, 370–380.

Sato, M., Shah, F.A., 2023. Contributions of resin cast etching to visualising the osteocyte lacuno-canalicular network architecture in bone biology and tissue engineering. Calcif. Tissue Int. 112, 525–542.

Schaepe, K., Bhandari, D.R., Werner, J., Henss, A., Pirkl, A., Kleine-Boymann, M., et al., 2018. Imaging of lipids in native human bone sections using TOF–secondary ion mass spectrometry, atmospheric pressure scanning microprobe matrix-assisted laser desorption/ionization orbitrap mass spectrometry, and orbitrap–secondary ion mass spectrometry. Anal. Chem. 90, 8856–8864.

Schneider, P., Meier, M., Wepf, R., Müller, R., 2011. Serial FIB/SEM imaging for quantitative 3D assessment of the osteocyte lacuno-canalicular network. Bone 49, 304–311.

Schulmerich, M.V., Finney, W.F., Popescu, V., Morris, M.D., Vanasse, T.M., Goldstein, S. A., 2006. Transcutaneous Raman spectroscopy of bone tissue using a non-confocal fiber optic array probe. In: Biomed. Vib. Spectrosc. III: Adv. Res. Ind., 60930O.

Schwarcz, H.P., 2015. The ultrastructure of bone as revealed in electron microscopy of ion-milled sections. Semin. Cell Dev. Biol. 46, 44–50.

Schwarcz, H.P., McNally, E.A., Botton, G.A., 2014. Dark-field transmission electron microscopy of cortical bone reveals details of extrafibrillar crystals. J. Struct. Biol. 188, 240–248.

Schwarcz, H.P., Abueidda, D., Jasiuk, I., 2017. The ultrastructure of bone and its relevance to mechanical properties. Front. Phys. 5, 39.

Schwarcz, H.P., Binkley, D.M., Luo, L., Grandfield, K., 2020. A search for apatite crystals in the gap zone of collagen fibrils in bone using dark-field illumination. Bone 135, 115304.

Shabestari, M., Eriksen, E.F., Paschalis, E.P., Roschger, P., Gamsjaeger, S., Klaushofer, K., et al., 2017. Presence of pyrophosphate in bone from an atypical femoral fracture site: a case report. Bone Rep. 6, 81–86.

Shah, F.A., 2020. Towards refining Raman spectroscopy-based assessment of bone composition. Sci. Rep. 10, 16662.

Shah, F.A., 2023. The many facets of micropetrosis – magnesium whitlockite deposition in bisphosphonate-exposed human alveolar bone with osteolytic metastasis. Micron 168, 103441.

Shah, F.A., Nilson, B., Brånemark, R., Thomsen, P., Palmquist, A., 2014. The bone-implant interface – nanoscale analysis of clinically retrieved dental implants. Nanomedicine 10, 1729–1737.

Shah, F.A., Wang, X., Thomsen, P., Grandfield, K., Palmquist, A., 2015a. High-resolution visualization of the osteocyte Lacuno-Canalicular network juxtaposed to the surface of nanotextured titanium implants in human. ACS Biomater Sci. Eng. 1, 305–313.

Shah, F.A., Johansson, B.R., Thomsen, P., Palmquist, A., 2015b. Ultrastructural evaluation of shrinkage artefacts induced by fixatives and embedding resins on osteocyte processes and pericellular space dimensions. J. Biomed. Mater. Res. A 103, 1565–1576.

Shah, F.A., Johansson, M.L., Omar, O., Simonsson, H., Palmquist, A., Thomsen, P., 2016a. Laser-modified surface enhances osseointegration and biomechanical Anchorage of commercially pure titanium implants for bone-anchored hearing systems. PLoS One 11, e0157504.

Shah, F.A., Snis, A., Matic, A., Thomsen, P., Palmquist, A., 2016b. 3D printed Ti6Al4V implant surface promotes bone maturation and retains a higher density of less aged osteocytes at the bone-implant interface. Acta Biomater. 30, 357–367.

Shah, F.A., Omar, O., Suska, F., Snis, A., Matic, A., Emanuelsson, L., et al., 2016c. Long-term osseointegration of 3D printed CoCr constructs with an interconnected open-pore architecture prepared by electron beam melting. Acta Biomater. 36, 296–309.

Shah, F.A., Zanghellini, E., Matic, A., Thomsen, P., Palmquist, A., 2016d. The orientation of nanoscale apatite platelets in relation to osteoblastic–osteocyte lacunae on trabecular bone surface. Calcif. Tissue Int. 98, 193–205.

Shah, F.A., Lee, B.E.J., Tedesco, J., Wexell, C.L., Persson, C., Thomsen, P., et al., 2017. Micrometer-sized magnesium whitlockite crystals in micropetrosis of bisphosphonate-exposed human alveolar bone. Nano Lett. 17, 6210–6216.

Shah, F.A., Thomsen, P., Palmquist, A., 2019a. Osseointegration and current interpretations of the bone-implant interface. Acta Biomater. 84, 1–15.

Shah, F.A., Ruscsák, K., Palmquist, A., 2019b. 50 years of scanning electron microscopy of bone – a comprehensive overview of the important discoveries made and insights gained into bone material properties in health, disease, and taphonomy. Bone Res. 7, 15.

Shah, F.A., Ruscsák, K., Palmquist, A., 2020. Transformation of bone mineral morphology: from discrete marquise-shaped motifs to a continuous interwoven mesh. Bone Rep. 13, 100283.

Shah, F.A., Jolic, M., Micheletti, C., Omar, O., Norlindh, B., Emanuelsson, L., et al., 2022. Bone without borders – monetite-based calcium phosphate guides bone formation beyond the skeletal envelope. Bioact Mater. 19, 103–114.

Skinner, H.C.W., 2005. Biominerals. Mineral. Mag. 69, 621–641.

Spevak, L., Flach, C.R., Hunter, T., Mendelsohn, R., Boskey, A., 2013. Fourier transform infrared spectroscopic imaging parameters describing acid phosphate substitution in biologic hydroxyapatite. Calcif. Tissue Int. 92, 418–428.

Stockhausen, K.E., Qwamizadeh, M., Wölfel, E.M., Hemmatian, H., Fiedler, I.A.K., Flenner, S., et al., 2021. Collagen fiber orientation is coupled with specific nano-compositional patterns in dark and bright osteons modulating their biomechanical properties. ACS Nano 15, 455–467.

Sundell, G., Dahlin, C., Andersson, M., Thuvander, M., 2017. The bone-implant interface of dental implants in humans on the atomic scale. Acta Biomater. 48, 445–450.

Surowiec, R.K., Allen, M.R., Wallace, J.M., 2022. Bone hydration: how we can evaluate it, what can it tell us, and is it an effective therapeutic target? Bone Rep. 16, 101161.

Systems OR, 2019. Dragonfly bone analysis. Available from: https://theobjects.com/dragonfly/bone-analysis.html (Internet, cited 2023 Dec 6).

Tang, S.Y., Zeenath, U., Vashishth, D., 2007. Effects of non-enzymatic glycation on cancellous bone fragility. Bone 40, 1144–1151.

Tang, T., Landis, W., Raguin, E., Werner, P., Bertinetti, L., Dean, M., et al., 2022. A 3D network of nanochannels for possible ion and molecule transit in mineralizing bone and cartilage. Adv. Nanobiomed. Res. 2, 2100162.

Tang, T., Landis, W., Blouin, S., Bertinetti, L., Hartmann, M.A., Berzlanovich, A., et al., 2023. Subcanalicular nanochannel volume is inversely correlated with calcium content in human cortical bone. J. Bone Miner. Res. 38, 313–325.

Taylor, E.A., Donnelly, E., 2020. Raman and Fourier transform infrared imaging for characterization of bone material properties. Bone 139, 115490.

Taylor, E.A., Mileti, C.J., Ganesan, S., Kim, J.H., Donnelly, E., 2021. Measures of bone mineral carbonate content and mineral maturity/crystallinity for FT-IR and Raman spectroscopic imaging differentially relate to physical–chemical properties of carbonate-substituted hydroxyapatite. Calcif. Tissue Int. 109, 77–91.

Tertuliano, O.A., Greer, J.R., 2016. The nanocomposite nature of bone drives its strength and damage resistance. Nat. Mater. 15, 1195.

Thorfve, A., Palmquist, A., Grandfield, K., 2014. Three-dimensional analytical techniques for evaluation of osseointegrated titanium implants. Mater. Sci. Tech. 31, 174–179.

Titchmarsh, J.M., 1989. Comparison of high spatial resolution in EDX and EELS analysis. Ultramicroscopy 28, 347–351.

Traub, W., Arad, T., Weiner, S., 1989. Three-dimensional ordered distribution of crystals in turkey tendon collagen fibers. Proc. Natl. Acad. Sci. USA 86, 9822–9826.

Tsurusawa, H., Nakanishi, N., Kawano, K., Chen, Y., Dutka, M., Leer, B.V., et al., 2021. Robotic fabrication of high-quality lamellae for aberration-corrected transmission electron microscopy. Sci. Rep. 11, 21599.

Uchic, M.D., Holzer, L., Inkson, B.J., Principe, E.L., Munroe, P., 2007. Three-dimensional microstructural characterization using focused ion beam tomography. MRS Bull. 32, 408–416.

Unal, M., Yang, S., Akkus, O., 2014. Molecular spectroscopic identification of the water compartments in bone. Bone 67, 228–236.

Utku, F.S., Klein, E., Saybasili, H., Yucesoy, C.A., Weiner, S., 2008. Probing the role of water in lamellar bone by dehydration in the environmental scanning electron microscope. J. Struct. Biol. 162, 361–367.

Verbeeck, J., Dyck, D.V., Tendeloo, G.V., 2004. Energy-filtered transmission electron microscopy: an overview. Spectrochim. Acta Part B: At. Spectrosc. 59, 1529–1534.

Wagermaier, W., Gupta, H.S., Gourrier, A., Burghammer, M., Roschger, P., Fratzl, P., 2006. Spiral twisting of fiber orientation inside bone lamellae. Biointerphases 1, 1.

Wang, Y., Ural, A., 2018. Effect of modifications in mineralized collagen fibril and extra-fibrillar matrix material properties on submicroscale mechanical behavior of cortical bone. J. Mech. Behav. Biomed. Mater. 82, 18–26.

Wang, Y., Euw, S.V., Fernandes, F.M., Cassaignon, S., Selmane, M., Laurent, G., et al., 2013. Water-mediated structuring of bone apatite. Nat. Mater. 12, 1144–1153.

Wang, X., Shah, F.A., Palmquist, A., Grandfield, K., 2017. 3D characterization of human nano-osseointegration by on-axis electron tomography without the missing wedge. ACS Biomater Sci. Eng. 3, 49–55.

Wang, M., Qian, R., Bao, M., Gu, C., Zhu, P., 2018a. Raman, FT-IR and XRD study of bovine bone mineral and carbonated apatites with different carbonate levels. Mater. Lett. 210, 203–206.

Wang, X., Langelier, B., Shah, F.A., Korinek, A., Bugnet, M., Hitchcock, A.P., et al., 2018b. Biomineralization at titanium revealed by correlative 4D tomographic and spectroscopic methods. Adv. Mater. Interfaces 5, 1800262.

Wang, X., Yang, J., Andrei, C.M., Soleymani, L., Grandfield, K., 2018c. Biomineralization of calcium phosphate revealed by in situ liquid-phase electron microscopy. Commun Chem. 1, 80.

Weiner, S., Traub, W., 1986. Organization of hydroxyapatite crystals within collagen fibrils. FEBS Lett. 206, 262–266.

Weiner, S., Wagner, H.D., 1998. The material bone: structure-mechanical function relations. Annu. Rev. Mater. Sci. 28, 271–298.

Weiner, S., Arad, T., Sabanay, I., Traub, W., 1997. Rotated plywood structure of primary lamellar bone in the rat: orientations of the collagen fibril arrays. Bone 20, 509–514.

Weiner, S., Raguin, E., Shahar, R., 2021. High resolution 3D structures of mineralized tissues in health and disease. Nat. Rev. Endocrinol. 17, 307–316.

Wierzchos, J., Falcioni, T., Kiciak, A., Woliński, J., Koczorowski, R., Chomicki, P., et al., 2008. Advances in the ultrastructural study of the implant–bone interface by backscattered electron imaging. Micron 39, 1363–1370.

Williams, D.B., Carter, C.B., 2009. Transmission Electron Microscopy. Springer, New York, NY.

Withers, P.J., Bouman, C., Carmignato, S., Cnudde, V., Grimaldi, D., Hagen, C.K., et al., 2021. X-ray computed tomography. Nat. Rev. Methods Prim. 1, 18.

Yerramshetty, J.S., Akkus, O., 2008. The associations between mineral crystallinity and the mechanical properties of human cortical bone. Bone 42, 476–482.

Zimmermann, E.A., Köhne, T., Bale, H.A., Panganiban, B., Gludovatz, B., Zustin, J., et al., 2015. Modifications to nano- and microstructural quality and the effects on mechanical integrity in Paget's disease of bone. J. Bone Miner. Res. 30, 264–273.